Draft version December 22, 2023
Typeset using LaTeX **twocolumn** style in AASTeX631

Photometric White Dwarf Rotation

Gabriela Oliveira da Rosa,[1] S. O. Kepler,[1] L. T. T. Soethe,[2,1] Alejandra D. Romero,[1] and Keaton J. Bell[3]

[1] *Instituto de Física, Universidade Federal do Rio Grande do Sul*
91501-970 Porto Alegre, RS, Brazil
[2] *Instituto Federal de Educação, Ciência e Tecnologia Sul-rio-grandense*
96745-000 Charqueadas, RS, Brazil
[3] *Department of Physics, Queens College, City University of New York,*
Flushing, NY, 11367, USA

ABSTRACT

We present a census of photometrically detected rotation periods for white dwarf stars. We analyzed the 9285 White Dwarfs observed by *TESS* telescope up to sector 69. We inspected the 21 832 light curves obtained for these stars using Fourier transform analyses and the *TESS-Localize* software to confirm the origin of the detected signals. As a result, we determined the rotation periods for 266 white dwarf stars. More than 60% of the stars composing our sample present a rotation period shorter than 10 h. Consequently, the median rotation period of our sample is 7.3 h, shorter than the median period reported in previous work. For stars in binary systems, we do not observe a preferential mass, temperature, or period. On the other hand, we observe that magnetic stars tend to present a higher mass, lower temperature, and shorter periods. Compiling all the rotation periods estimated through asteroseismology and reported until now, we found that seismological rotation periods exhibit a distribution similar to the distribution of our photometric sample. We also reported non-pulsating periods we detected in *TESS* data for three known pulsating WDs. In addition, we also calculated evolutionary models including six angular momentum transfer mechanisms from the literature, including the Spruit-Tayler dynamo, throughout the evolution, in an attempt to reproduce our findings. Our models indicate that the temperature-period relation of most observational data is best fitted by not activating the angular momentum transport mechanism in models with initial rotational velocity 50 km s^{-1} and $Z = 0.02$ metallicity, or in models with $Z = 0.001$ metallicity and initial rotational velocity 10 km s^{-1}. Previous models had already shown that the angular momentum transfer mechanism necessary to explain the observed rotation rates in red giants had to be turned off in the models after helium burning to achieve rotation rates of the order of days at the white dwarf phase. It is unlike that no transport occurs and that the metallicities are low, so the model assumptions are inadequate.

INTRODUCTION

The rotation period is an essential parameter for the study of stellar evolution. It plays a significant role in the stellar dynamo mechanism and is directly related to the mass loss experienced by stars during the asymptotic giant branch (AGB). For both single stars and stars in binary systems, photometry allows us to detect the rotation period of stars directly and indirectly through asteroseismology.

Binary stellar systems can exhibit light variability due to different effects. Depending on the geometry of the system and the orientation of the orbital plane as observed from Earth, light variability from binary systems can provide the rotational period of stars or the system's orbital period. Variability resulting from ellipsoidal variation or reflection in binary systems provides stellar rotation periods, whereas variability from orbital motion indicates the system's orbital period (e.g. Krtička et al. 2023). However, in the case of spin-orbit coupling, there is no difference between orbital and rotational periods. The spin-orbit coupling occurs when there is mass loss due to winds, trying to balance the variation in the spin of each star with the angular momentum of the system. Zahn (1977) demonstrated that the synchronization time between stellar rotation and orbital period of a binary system is proportional to $P_{\rm orb}^4$, where $P_{\rm orb}$ is the orbital period of the system. This implies that the shorter the orbital period, the faster the synchronization process occurs. Zahn (1977), suggests that periods smaller than 17 days are synchronized.

Single stars, like our Sun, may also exhibit light variability because of the presence of dark spots and patches on their surface. These inhomogeneities are typically associated with the presence of a magnetic field or with a variation in the chemical composition across the stellar surface (e.g. Babcock 1960; Kochukhov 2011). In this case, the rotation period as well as some harmonics can be present in the light curves, depending on the number of spots.

Luminosity variations due to rotation are detected in white dwarf stars in single and multiple systems. White dwarf (WD) stars are the most common end of stellar evolution, constituting the fate of $95 - 97\%$ of all stars in the Galaxy (e.g. García-Berro et al. 1997; Poelarends et al. 2008; Siess 2010; Langer 2012; Woosley & Heger 2015; Doherty et al. 2014). As fossils, WDs preserve valuable information about their past evolution, making them essential for studying the structure, evolution, chemical enrichment, and star formation history of our Galaxy (Diaz-Pinto et al. 1994). WDs are classified into spectral classes based on the dominant chemical element on their surface. Approximately 80% of all WDs belong to the DA spectral type (e.g. Kepler et al. 2021), with the spectra showing only hydrogen (H) lines. The remaining 20% mainly consist of WD stars of spectral types DB and DO, featuring helium-dominated atmospheres. DOs are characterized by spectra with high-excitation lines of He II, C IV, O VI, and N V, and $T_{\rm eff}$ exceeding $40,000$ K.

Although WDs have been studied since 1915 (Adams 1915), their rotation period distribution is still largely undetermined. Ground-based observations cannot easily measure rotation periods because of atmospheric and instrumental limitations, as WDs are intrinsically faint stars. Furthermore, the time gap due to daylight constrains the period range that can be determined (Nather et al. 1990). Long-time baseline observations from space-based telescopes have largely overcome the latter problem. The *Kepler* spacecraft was launched in 2009, obtaining excellent data to search for stellar variability (e.g. Molnár et al. 2016). The failure of its second reaction wheel in 2013 caused significant noise problems at low frequencies. It presented a serious challenge in identifying rotation periods for faint stars. The launch of the *TESS* telescope in 2018 (201 2014) allowed a reliable analysis of low frequencies for WD stars. Even with many gaps, the *TESS* data enabled the detection of photometric rotation periods directly in the frequency spectrum (e.g. Labadie-Bartz et al. 2023).Finally, the high-precision astrometry obtained by the Gaia mission (Gaia Collaboration et al. 2018), has considerably improved the determination of the parallax and photometry of stars.

Alternatively, it is also possible to estimate the stellar rotation period of stars through asteroseismology by studying their pulsation period spectra, as in Kepler & Romero (2017). For example, Hermes et al. (2017b) estimated the rotation period for twenty WDs, all pulsating hydrogen atmosphere DAVs, using data from the *Kepler* spacecraft. The authors combined these results with the early estimates compiled by Kawaler (2015), and found a mean rotation period of 35 ± 28 h for a sample of 40 objects, with a slight tendency to shorter periods for higher masses.

This work presents the first analysis of the rotation period distribution of a large sample of WD stars based on photometric data from the TESS telescope. We analyzed 21 832 light curves of the 9285 white dwarfs observed by *TESS* from sectors 1 to 69. We searched for stable variability and used the *TESS-Localize* software to confirm the signal source, as presented in Section 1. In Section 2, we present the results for the rotation period distribution for 266 WDs and analyze its dependence on the stellar parameters. In this section, we also report the non-pulsating periods we detect for three known pulsating WDs. In Section 3, we perform theoretical model computations to analyze the effects of different angular momentum transfer mechanisms present during the WD evolution. Finally, we present our concluding remarks in Section 6.

1. DATA ANALYSIS

We selected all known WDs, including Gaia candidates from Gentile Fusillo et al. (2021), and matched them with the *TESS* telescope data for objects up to magnitude $G = 17.5$. This process yielded a sample of 9285 stars. We analyze the 21 832 light curves available for all 9285 white dwarfs observed with *TESS* from sectors 1 (starting 25 July 2018) to 69 (ending 20 September 2023). We used the *Lightkurve* package (Lightkurve Collaboration et al. 2018) to download the photometric data observed by *TESS*. We selected the data taken with a cadence of 120 s (and 20 s when available) and processed using the SPOC pipeline (Caldwell et al. 2020). *TESS* telescope observes each sector for 27 days, interrupting the observation each ~ 13 days - or less - to send the data to Earth. Due to these gaps in the light curve, we searched for stable variability only up to 12 days. To avoid including pulsation periods, we also checked linear combinations and whether the temperature of the candidate star with periods shorter than 1500 s matched the temperature range of the DOV, DBV, and DAV/ELMV white dwarf instability strips.

We combined the light curves of all sectors in which the star was observed and performed a complete Fourier transform (FT) on it. We also computed the false alarm probability (fap) of 1/1000, that is, the limit beyond which peaks on the Fourier transforms have less than one chance in 1000 of being noise. We use this detection limit to define whether the observed signal is significant. The fap is computed by randomizing (Monte Carlo-like simulation) the observed timings, as described in Kepler (1993). If the FT exhibited any peak with an amplitude above the detection limit, we considered the period with the highest amplitude as a potential variability signal of the WD. When confronted with the detection of multiple harmonic frequencies in the FT, we analyzed the shape of the dips in brightness and examined the light curve folded in phase. When a noisy light curve hindered the observation of the shape of the variability curve, our approach was to select the harmonic peak with the lowest frequency. Following these criteria, we compile a target list of 843 WDs with a detected variability frequency.

We identified within the WDs that make up our sample those with detected magnetic field, as well as those in binary systems. For magnetic WDs, we first used the classification from the catalog Amorim et al. (2023) and then the literature for other objects (e.g., McCook & Sion 2016; Wenger et al. 2000; Kepler et al. 2021; O'Brien et al. 2023; Tremblay et al. 2020; Kilic et al. 2020; Guo et al. 2022). We used the classification of WDs in binary systems from the literature. We also detected new systems by inspecting the Gaia proper motion and parallax data within a box of 120″ around the white dwarf.

In addition, we compiled all the 51 WDs with rotation periods determined by asteroseismology up to now and matched them with *TESS* data. For the 36 pulsating WD observed by *TESS*, we inspect all the light curves searching for reliable non-pulsating periods. Using the Pyriod Fourier analysis software (Bell 2020), we detect the variability frequencies and subtract their respective sinusoids from the light curves of *TESS* (pre-whitening). We estimated the false-alarm probability (fap) of 1/1000 by randomization. To check the presence of a rotation period in the FT, we identified the pulsation frequencies as well as their linear combination. After this process, we got a list of 14 pulsating WDs with candidate periods.

1.1. *Localizing the signal*

The *TESS* telescope offers long-time light curves and high-frequency resolution. However, because of its large plate scale of $21''\mathrm{px}^{-1}$, it exhibits a low spatial resolution. Consequently, signals from nearby sources contaminate many *TESS* light curves. We overcome this problem using *TESS-Localize* software (Higgins & Bell 2023) to determine whether the detected period arises from the WD or a nearby star. For each star in our target list, we run *TESS-localize* for all sectors in which the star was observed, setting the *Principal Components* parameter to 3 (see Higgins & Bell 2023).

There are two crucial *TESS-Localize* output parameters that need to be checked to ensure the quality of the fit: *Height* and *p-value*. When *TESS-Localize* fits the signal positions, the strength of the signals is represented as the best-fit *Height* parameter. Similarly to the challenge of identifying stars in an image, the signal needs to stand out significantly from the background noise. Higgins & Bell (2023) recommends that the *Height* parameter exceed five times its uncertainty for the localization to be considered significantly above the noise floor. Another critical parameter is the *p-value*; this number supports the hypothesis that the location of the fit of the signal is consistent with the position of the source. Because we do not discard this hypothesis, the *p-value* should be reasonably high. We adopt the same threshold as Pedersen & Bell (2023): $'p-value' \geq 0.05$. Applying these criteria, we selected only those sectors for which *TESS-Localize* achieved a significant localization of the signal of interest that is consistent with the location of a known *Gaia* source brighter than $G = 18\,mag$. Therefore, since we excluded noisy sectors, we do not need to be concerned about the variation in noise from sector to sector.

The final constraint step involves an examination of the *Relative Likelihood*, also an output parameter of *TESS-Localize*. It essentially ranks the proximity of Gaia sources to the localized position of the signal within the pixels. For the same target, *TESS-Localize* can fit distinct values of *Relative Likelihood* for each available sector of data. So, for analysis purposes, we denoted the mean *Relative Likelihood* over all selected sectors as *Like*. To be consistent, we only consider that the signal originates from the WD if *TESS-Localize* indicates the WD as the most probable source for all selected sectors. To demonstrate the consistency of our results, we imposed different thresholds on *Like* and *Amplitude* of the detected signals, creating four distinct samples. Given that the software estimates $Like \simeq 0.75$ for some known variables (see Appendix A - Known RR Lyrae Star), *Sample 1* was selected by applying $Like \geq 0.75$. One might think 75% is not enough, so we propose *Sample 2* with a stricter criterion on *Like*, selecting only candidates with $Like \geq 0.99$. *Sample 3* was chosen considering the fact that *TESS-Localize* was tested only for signals with an *Amplitude* greater than 7σ (7 times the mean Amplitude of the FT). Lastly, to affirm the re-

liability of our finding, even considering the extremely high variability, we selected *Sample 4* imposing an even more rigorous *Amplitude* criterion of 10σ.

The *TESS-Localize* analysis with strict conditions reduced by 70% our initial sample of 843 candidate stars. *Sample 1* consists of 266 WD, including 64 in binary systems and 15 that have detected magnetic fields. Further details of the samples are available in Table 1, which summarizes information on the applied selection thresholds, the quantities of white dwarfs, binaries, and magnetic stars in each sample, along with their median periods. Table 5 in Appendix C - Rotational Periods Table lists all stars that compose our samples, informing its variability period, amplitude, *Like*, mean *Height* parameter normalized by uncertainty, temperature, mass, and additional information. Table 5 also reports the fraction of sectors whose *TESS-Localize* fit achieved our quality criteria as 'Q/S'.

We applied this same analysis using *TESS-Localize* for the periods of the selected pulsating WDs. We found that the WD is the source of the non-pulsating periods we detected only for 3 of 14 candidate stars. Table 3, in Section 3.1, presents the details of the non-pulsating periods we identified, including amplitude, and quality parameters from the *TESS-Localize* fit.

2. PHOTOMETRIC ROTATION PERIODS

In this section, we present the results for the rotation period distribution for the 266 WDs. Assuming that any inhomogeneity on the stellar surface will manifest itself as variability with the rotation period of the surface, from now on, we will attribute the detected variability periods to rotation. This consideration follows the exclusion of all periods potentially caused by pulsation. As mentioned in Introduction, we expect that the rotation period and the orbital period for binary systems with orbital periods shorter than 17 days are synchronized. Therefore, since the observed periods are shorter than 12 days, we assumed that all binary systems in our sample are synchronized.

Before we present our results, as an example, Figure 1 shows the Time series analysis for one of the WDs for which we have determined the rotation periods. The top panel displays the FT of the star 'TIC 1507548590', where the red dashed line indicates the fap. The FT presents two significant peaks: a frequency corresponding to 1.92772 hours and its harmonic. The bottom panel of Figure 1 shows the folded light curve for the highest period detected in the FT, confirming that this is the period corresponding to the rotation of the star.

2.1. *Mass and Temperature Distribution*

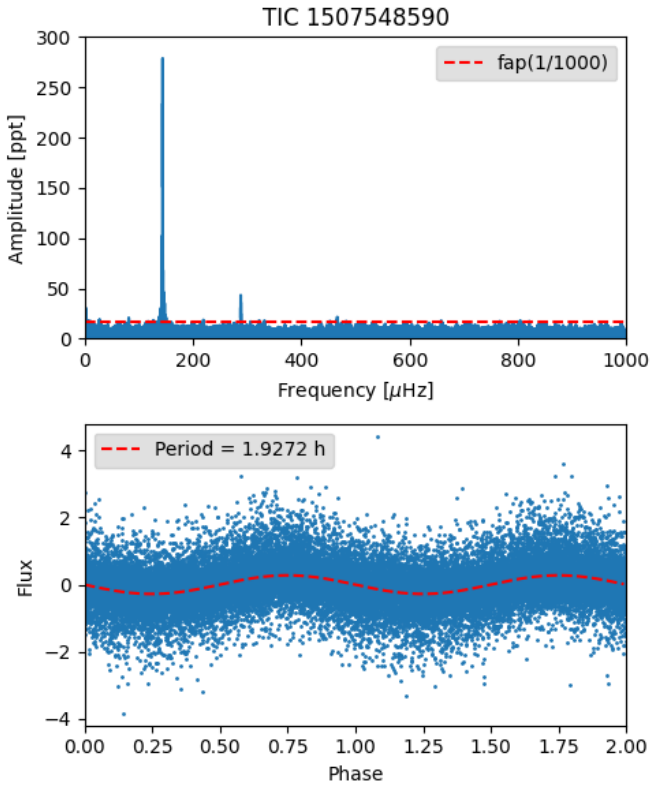

Figure 1. Time series analysis for the star 'TIC 1507548590'. The top panel shows the Fourier Transform as well as its false alarm probability (red dashed line). The bottom panel shows the light curve folded on the period of 1.92772 hours and a sinusoid curve with the same period in red.

As the *Sample 1* encompasses all others, we will use it as a reference sample to analyze the mass and temperature distributions. Figures 2 (3) show the dependence of the rotation period -in a logarithmic scale- on the stellar mass (effective temperature), in the left panel, and the histogram of the period distribution in the right panel. The red points and bins denote magnetic WDs, whereas the blue points correspond to WDs in binary systems.

The histogram in Figure 2 shows a distribution centered around approximately 0.6 $M_\odot$ and, standing out from this distribution, there is the 0.2 $M_\odot$ bin (the highest). The distribution around 0.6 $M_\odot$ is consistent with the values expected for the mass distribution of WDs (O'Brien et al. 2023). On the other hand, the peak at 0.2 $M_\odot$ contains 18% of the sample and cannot be explained by the evolution of a single star. It is probably caused by an observational bias. WDs with a mass lower than 0.45 $M_\odot$ are formed by binary interaction (e.g. Marsh et al. 1995; Kilic et al. 2007) since it would take longer than the age of the universe for them to evolve as single stars. It is also important to note that there is

	Thresholds	Stars	Binaries	Magnetic	Median Period (h)
Sample 1	*Like* ≥ 0.75	266	64	15	7.30
Sample 2	*Like* ≥ 0.99	242	52	15	6.92
Sample 3	*Like* ≥ 0.99 and Amplitude $\geq 7\sigma$	196	49	9	7.99
Sample 4	*Like* ≥ 0.99 and Amplitude $\geq 10\sigma$	163	45	6	7.90

Table 1. Compilation of our samples' information: their stellar composing, the thresholds used to select them, and their median period.

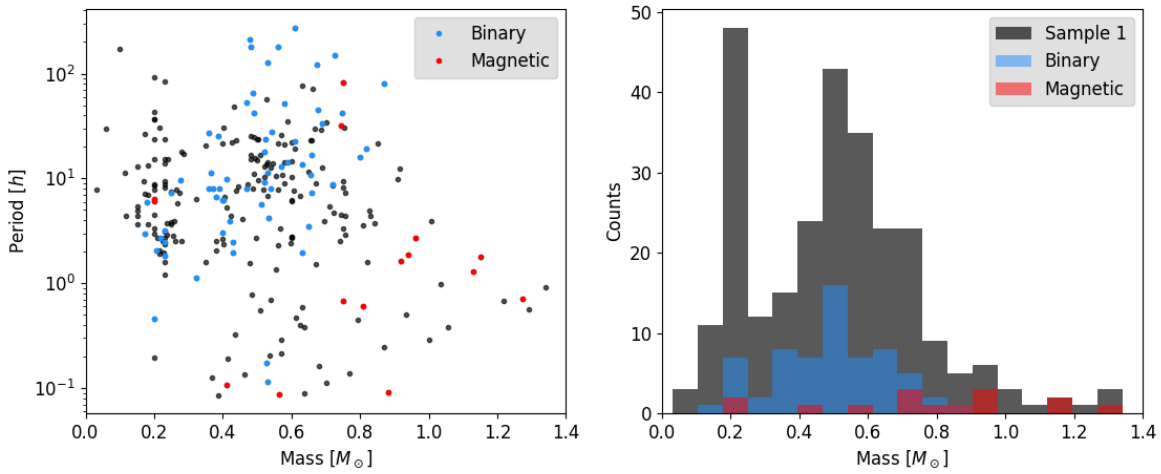

Figure 2. The left panel displays the rotational period in hours in log scale versus mass in solar masses, while the right panel shows the mass distribution of sample 1. The red dots/bins represent magnetic, while blue represents white dwarfs in binary systems, respectively.

a selection effect on the determination of the mass. WD spectrum contaminated by an unresolved red star commonly leads to a mass determination of approximately $0.2M_\odot$. If this is the case, the peak at $0.2M_\odot$ in our mass distribution is probably overestimated.

Even with that in mind, the plot on the left of Figure 2 shows that short periods are not dominated by low-mass WDs. Instead, they are distributed throughout the WD mass range. Low-mass WDs exhibit a wide range of rotation periods, ranging from approximately 100 hours to less than an hour. Actually, we observe this variety of rotation periods along almost the entire mass range, except for masses larger than $\sim 1M_\odot$, where we have few targets.

The left panel of Figure 2 also shows that most magnetic WDs in our sample exhibit periods shorter than 7 h and that they are among the targets with the shortest periods. It is essential to recognize that our sample has selection effects. According to Brinkworth et al. (2013), the rotational period of magnetic white dwarfs exhibits a bimodal distribution, with one group showing periods on the order of minutes to hours and the other displaying periods much longer than their 4 years. However, their total sample is made up of only 26 stars. Each observation cycle (sector) of the *TESS* telescope lasts $\approx$ 27 days, with a data transfer interruption in the middle, limiting the detection of periods to a few hundred hours. In this way, we are detecting only a portion of magnetic WDs. Furthermore, massive WDs are fainter and tend to rotate more rapidly (e.g., Hermes et al. 2017b; Caiazzo et al. 2021; Williams et al. 2022). Although *TESS* is a small telescope, most of our magnetic sample consists of massive white dwarfs rotating with periods shorter than 3 hours, as Figure 2 shows.

Figure 3 shows that our sample of white dwarfs is distributed around approximately 12,000 K, a representative value of the DA population, which comprises about 80% of the WDs identified spectroscopically (e.g. Kepler et al. 2021). The left panel of Figure 3 shows that there does not appear to be a dependence of the rotation period on the effective temperature.

Furthermore, there is no obvious dependence of the rotation period on the stellar mass or the effective temperature of the white dwarf for binary systems. However, despite the selection effects, the magnetic white dwarfs in our sample tend to be located at higher masses and lower temperatures, probably because of their longer cooling times (Kepler et al. 2021).

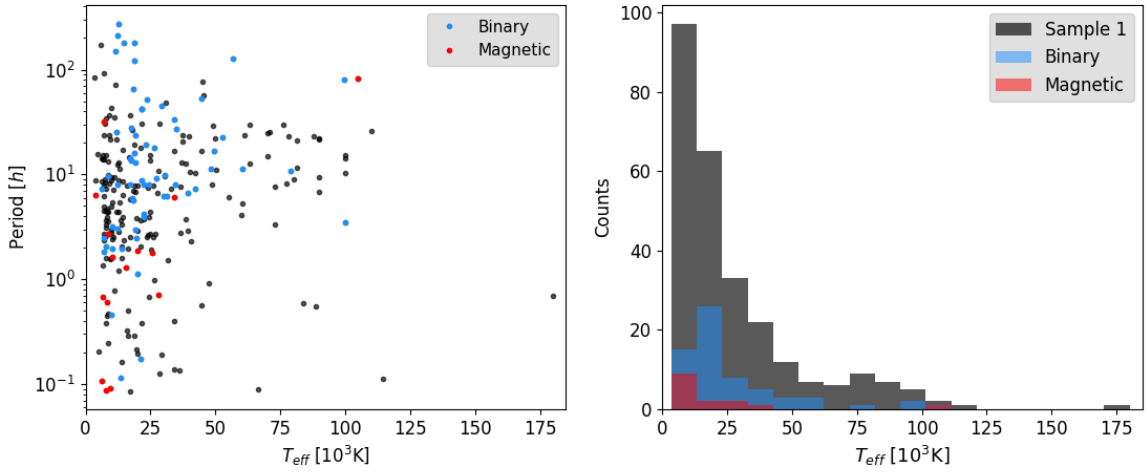

Figure 3. The left panel displays the rotational period in hours versus the effective temperature in Kelvin, both in log scale. The right panel shows the temperature distribution of sample 1. The red and blue dots/bins represent magnetic and binary white dwarfs, respectively.

2.2. *Rotation Period Distribution*

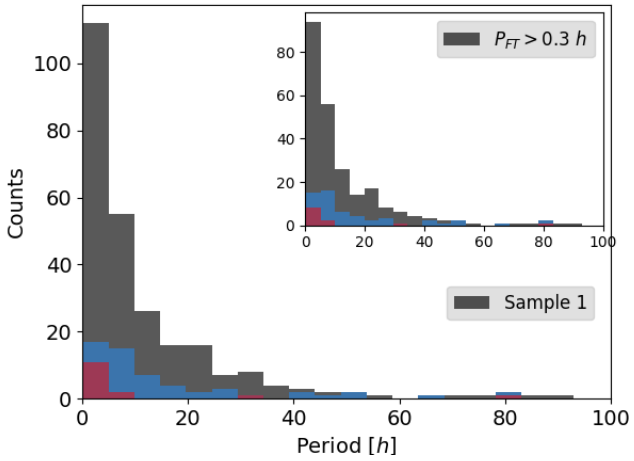

Figure 4. Rotation period histogram of sample 1. The inset plot illustrates the rotation period histogram excluding periods shorter than 0.3 h. Blue bins indicate WD in binary systems, and red bins indicate magnetic WDs.

Figure 4 shows the distribution of rotational periods for sample 1 up to 100 h. As explained in section 1, we excluded pulsation periods. However, to eliminate any doubts about the short periods in our sample, the inset of Figure 4 shows the histogram of periods longer than 0.3 h. It is important to note that massive white dwarfs can exhibit rotation periods shorter than 0.3 h (e.g. Caiazzo et al. 2021; Barstow et al. 1995). The inset plot confirms that even if we are quite conservative, most of our sample still has rotation periods shorter than 10 h.

Figure 5 shows the complete histograms of the rotational periods (right) and the histograms of periods up to 30 h (left) for our four samples. Each line of this figure displays the histograms of one sample, indicated by the respective subtitles. The first line presents the histograms of *Sample 1*, the second line presents the histograms of *Sample 2*, and so on. The last line of Figure 5 shows the same histogram but for the rotational periods determined through asteroseismology, which are listed in Table 2. The red and blue bins represent the magnetic WDs and the WD in binary systems.

The right panels of Figure 5 show that more than 60% of the targets fall into the shortest period bin for all four of our samples. It shows that regardless of the restrictions chosen in our initial sample, the data remain indicating the same result: most WDs have a rotational period shorter than approximately 10 h. The left panels of Figure 5 display the same histograms but periods up to 30 hours. They show that the stricter the threshold over the sample, the more prominent the distribution of periods around three distinct values: approximately 3 h, 8 h, and 24 h.

Looking at the right panel of the last line, we see that the distribution of the seismological periods is a little different from the distributions of our samples. Despite the smaller sample size, its shortest period bin is not as prominent as we observed in the distributions of our samples. Instead, the seismological distribution presents almost as many periods shorter than 13 h (14) as periods between 25 and 37 hours (13). The seismological histogram presents a bimodal distribution around the first bin (periods shorter than 13 hours) and approximately 31 hours. Looking at the short periods, the last

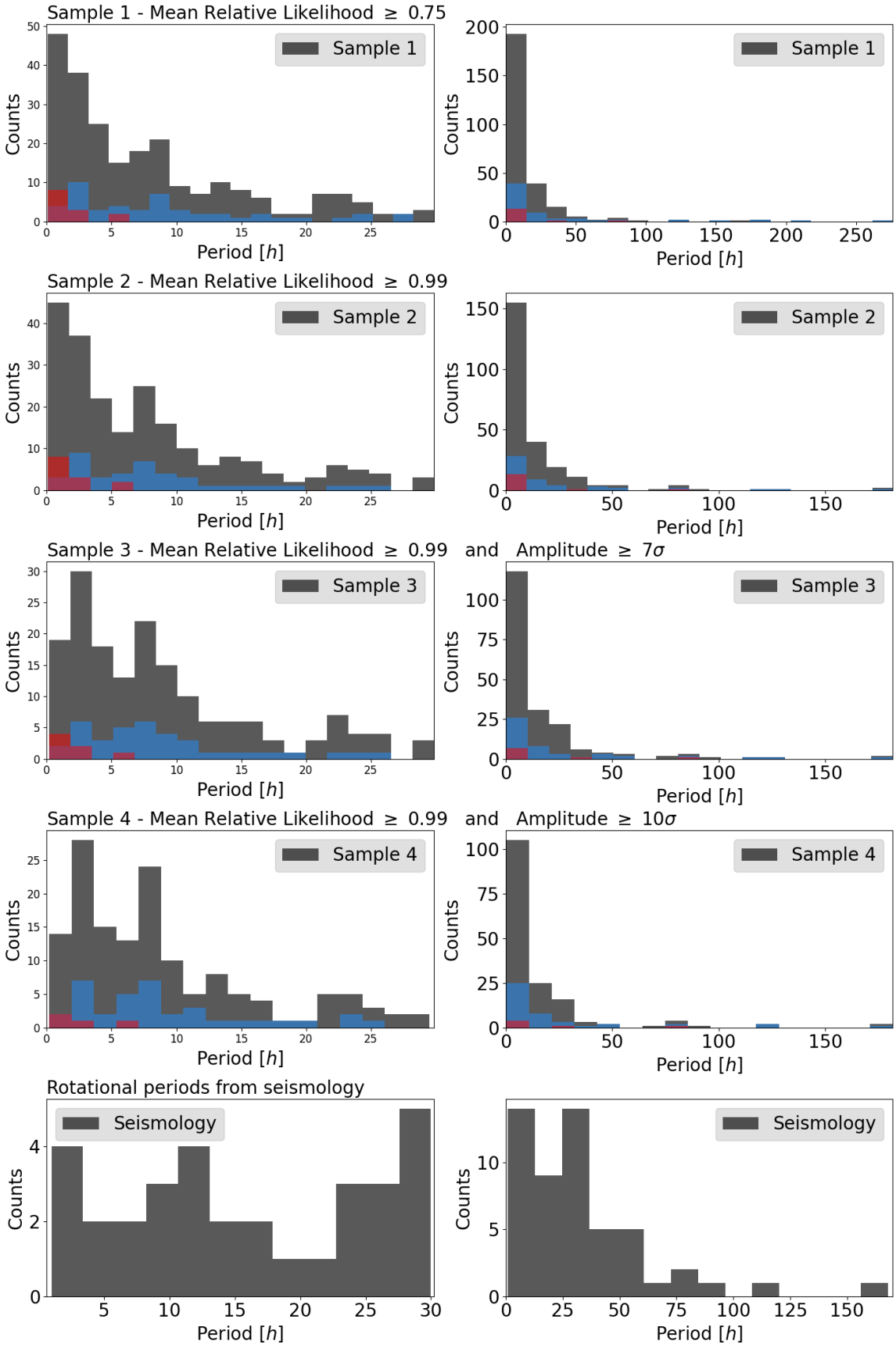

Figure 5. Rotation period histograms for different thresholds over *TESS* data and, last line, histograms of rotation periods from seismology. On the left, we present the histograms of rotation periods up to 30 h, and on the right, the complete histograms. The red and blue bins show, respectively, the binary and magnetic population in our sample of WDs.

line of Figure 5 reveals that the asteroseismological periods are also distributed around three values. Similarly to those observed in our samples, the seismological histogram is distributed around approximately 2 h, 12 h, and 31 h.

Figure 5 also shows that the fraction of WD in binary systems with periods shorter than 30 h increases as we restrict our sample. Looking at the period distribution for binaries, they do not exhibit a preferential value; instead, they are evenly distributed. It is challenging to draw definitive conclusions about magnetic white dwarfs due to the small sample size. Despite this limitation, Figure 5 points in the direction where magnetic WDs tend to be fast rotators, since most have rotational periods shorter than 6.4 h.

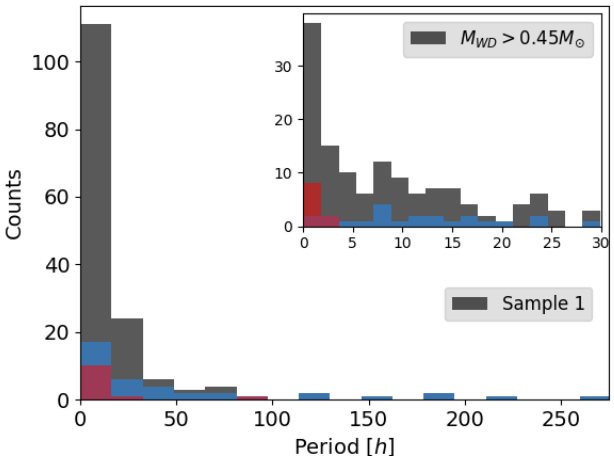

Figure 6. Rotation period histogram of sample 1 excluding target stars with a mass lower than 0.45 $M_\odot$. The principal plot illustrates the entire histogram of rotation periods, and the inset plot the histogram with periods up to 30 h. Blue bins indicate WD in binary systems, and red bins indicate magnetic WDs.

Figure 6 shows the distribution of rotational periods only for stars with mass higher than 0.45 $M_\odot$. The principal graph presents the entire histogram of periods, while the inset plot presents the histogram for periods up to 30 h. This plot confirms that even if the variability we found for the low-mass WDs were all due to ellipsoidal variations, this is not what is causing the short periods in our samples. However, Figure 6 shows that excluding low-mass WDs from our sample emphasized the importance of the shortest period bin.

3. PULSATING WHITE DWARFS

3.1. *Rotation periods from asteroseismology*

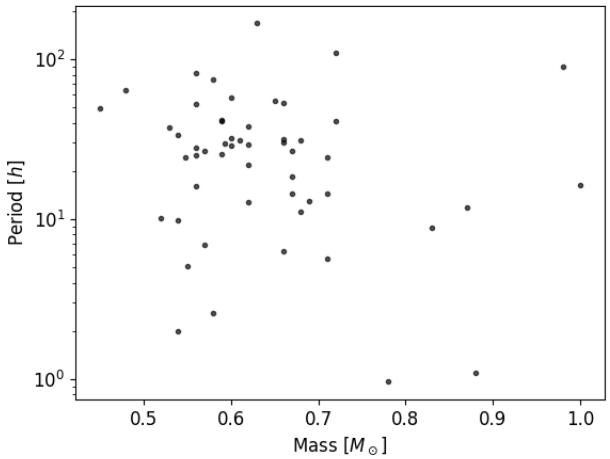

Figure 7. Rotation period versus mass relation for period determinations from asteroseismology. The period axe is in log scale.

As mentioned in Introduction, Kawaler (2015), Hermes et al. (2017b) and Kepler & Romero (2017) reported the rotation period of WD using determinations from asteroseismological analysis. Extending their work, we compile all 53 WDs stars with reported seismological rotation periods up to the present. They are listed in Table 2. We have already shown the histogram of the seismological periods in Figure 5. They present a median rotational period of 27 hours and a standard deviation of 30 hours. Investigating the trend of decreasing rotation period with increasing white dwarf mass claimed by Hermes et al. (2017b), we present Figure 7 which shows the rotation period versus mass relation for the seismological sample. The current plot does not show this trend; instead, the two most massive stars in our sample exhibit rotation periods longer than 10 hours.

3.2. *Non-pulsating periods*

From the 51 stars listed in Table 2, 36 was observed by **??**. We analysed all of them searching for non-pulsating periods. Most pulsating WDs do not exhibit any frequency with amplitude above the detection limit, other than pulsation periods, or show only low amplitude at frequencies smaller than 4.6 μHz (10 times the frequency resolution of a sector) in the FT. Some pulsating WDs exhibit dozens of pulsation frequencies in their FTs, leading to linear combinations at low-frequency. We only identified variability periods outside the pulsation range for three of these stars: NGC 1501, TIC 7675859, and G 226-29. These objects are described in the following Sections 3.2.1, 3.2.2 and 3.2.3. Their *TESS-Localize* output parameters are compiled in Table 3.

Star	$P_{\rm seism}$ [h]	Type	Mass [$M_\odot$]	Ref.	Star	$P_{\rm seism}$ [h]	Type	Mass [$M_\odot$]	Ref.
TIC 7675859	6.34	DAV	0.66	0	TIC 343296348	24.48	DAV	0.548	1
TIC 21187072	53.76	DAV	0.66	1	TIC 394015496	29.76	DAV	0.593	1
PG 1159-035	33.6	DOV	0.54	2	RX J2117.1+3412	25	DOV	0.56	3
GD133	168	DAV	0.63	4	EPIC220274129	12.7	DAV	0.62	5
PG 0112+104	10.2	DBV	0.52	6	KIC 4552982	18.4	DAV	0.67	7
KIC 4357037	22	DAV	0.62	7	KIC 7594781	26.8	DAV	0.67	7
KIC 10132702	11.2	DAV	0.68	7	EPIC60017836	6.9	DAV	0.57	7
EPIC201719578	26.8	DAV	0.57	7	EPIC201730811	2.6	DAV	0.58	7
EPIC201802933	31.3	DAV	0.68	7	EPIC210397465	49.1	DAV	0.45	7
EPIC211596649	81.8	DAV	0.56	7	EPIC211629697	64	DAV	0.48	7
EPIC211914185	1.1	DAV	0.88	7	EPIC211926430	25.4	DAV	0.59	7
EPIC228682478	109.1	DAV	0.72	7	EPIC229227292	29.4	DAV	0.62	7
EPIC220204626	24.3	DAV	0.71	7	EPIC220258806	30	DAV	0.66	7
EPIC220347759	31.7	DAV	0.66	7	EPIC201806008	31.3	DAV	0.61	7
KUV02464+3239	90.7	DAV	0.98	8	SDSS J0349-0059	9.8	DOV	0.54	9
GD 165	57.3	DAV	0.6	10	Ross 548	37.8	DAV	0.62	10
PG1707+427	16	DOV	0.56	11	WD 1711+657	16.4	DAV	1.00	11
GD 358	29	DBV	0.6	11	G29-38	32	DAV	0.6	11
EC20058-5234	2	DBV	0.54	11	EC14012-1446	14.4	DAV	0.71	11
KIC 11911480	74.7	DAV	0.58	12	WD 0937+010	11.8	DAV	0.87	13
SDSS J1612+830	0.96	DAV	0.78	13	KUV11370+4222	5.7	DAV	0.71	14
GD 154	55.2	DAV	0.65	15	HS 0507+0434	40.9	DAV	0.72	15
KIC 8626021	40.8	DBV	0.59	16	PG 0122+200	37.2	DOV	0.53	17
HL Tau 76	52.8	DAV	0.56	18	G185-32	14.5	DAV	0.67	19
L19-2	13.0	DAV	0.69	20	LP 133-144	41.8	DAV	0.59	21
NGC 1501	28.1	DOV	0.56	22	G226-29	8.9	DAV	0.83	23
PG 2131+066	5.1	DOV	0.55	24					

Table 2. White dwarfs with rotation periods determined previously by asteroseismology.
References: (0) This work; (1)Romero et al. (2022);(2)Oliveira da Rosa et al. (2022); (3)Córsico et al. (2021a);(4) Fu et al. (2019);(5) Bell et al. (2017); (6) Hermes et al. (2017a); (7) Hermes et al. (2017b); (8) Li et al. (2017); (9) Calcaferro, Leila M. et al. (2016); (10) Giammichele et al. (2016); (11) Kawaler (2015); (12) Greiss et al. (2014); (13) Castanheira et al. (2013); (14) Su et al. (2013); (15) Fu et al. (2012); (16) Østensen et al. (2011); (17) Fu, J.-N. et al. (2007); (18) Dolez, N. et al. (2006); (19) Pech, D. & Vauclair, G. (2006); (20) Bradley (2001); (21) Pfeiffer et al. (1996); (22) Bond et al. (1996a); Kepler et al. (1995a); (23) Kawaler et al. (1995).

3.2.1. *NGC 1501*

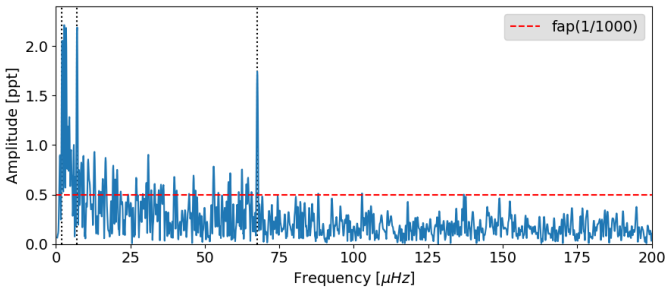

Figure 8. Fourier transform of *NGC 1501* data at low frequencies.

The pulsating $T_{\rm eff} = 134\,000 \pm 10\,000$ K, $\log g = 6.00 \pm 0.20$ pre-white dwarf NGC 1501 was discovered to pulsate with periods from 5235 s to 1154 s, with the largest amplitudes at 1318.46 ± 0.07 s@5.05 ± 0.36 mma and 1154.36 ± 0.06 s@5.00 ± 0.37 mma, by Bond et al. (1996b). They estimate a rotation period of 1.17 days from a mean splitting of 9.9 μHz. It was observed by TESS during sector 19 for 25 days with 120 s exposures. Analyzing its FT, we detected three variability frequencies from the WD star (see Figure 8) corresponding to 4.11, 39, and 138 hours, and the 15 pulsation periods listed in Table 6 of Córsico et al. (2021b). *NGC 1501* is a planetary nebula covered by an ionized gas disk. Its seismology was recently studied by Córsico et al.

Name	TIC	FT Period [h]	Amplitude [σ]	Like	$\langle$ Height [σ] $\rangle$	Q/S
NGC 1501	84306468	138 ± 32	15.377	1.0	7.46	1/1
		39 ± 2	18.104	1.0	18.4	1/1
		4.11 ± 0.03	14.571	1.0	15.4	1/1
TIC 7675859	7675859	12.344 ± 0.008	8.768	1	8.1	5/6
G226-29	199666369	0.93 - 3.25	4.129 - 13.934	1.0	9.4	27/29

Table 3. Non-pulsating periods from pulsating white dwarfs.

(2021b). Figure 8 shows the FT of *TESS* data up to $200\mu Hz$, the three non-pulsating periods we have detected are marked with dotted vertical lines.

3.2.2. *TIC 7675859*

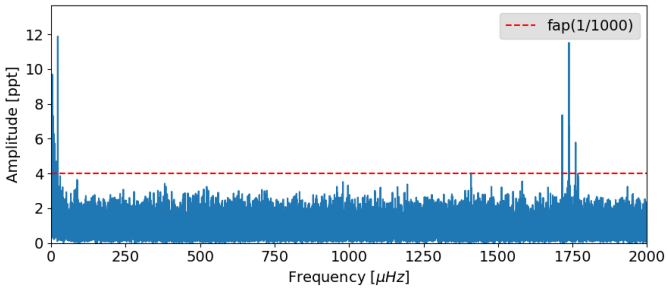

Figure 9. Fourier transform of *TIC 7675859* data from sectors 52 to 54.

Romero et al. (2022) determined the asteroseismological rotation period of *TIC 7675859* based on data from sectors 25 and 26. Since then, the DAV has also been observed in sectors 40, 52, 53, and 54. In the 25 and 26 sector data, only two triplet components have a high confidence level. Fortunately, we observed the three components of a high amplitude triplet in the data of sectors 52 to 54 (see Figure 9), allowing for a more precise fit. The triplet at $1738\mu Hz$ shown in Figure 9 is perfectly symmetric with a frequency spacing $\Delta\nu = 22.47$ μHz. With this splitting, we can calculate the rotation period by the Ledoux equation:

$$\frac{1}{P_{seis}} = \frac{\Delta\nu}{1 - C_{k,\ell}}$$

where $C_{k,\ell}$ is the rotational splitting coefficient. Using $C_{k,\ell}$ estimated by Romero et al. (2022) (0.487), we get a rotation period of 6.34 ± 0.04 h.

Moreover, we observe a significant peak in the *TESS* FT at 22.44 μHz (corresponding to 12.3 h), which is a very close value to the mean frequency spacing of this triplet (22.47 μ Hz). The peak at 22.44 μHz is higher than all components of the triplet at $1738\mu Hz$, however, we cannot eliminate the possibility that it is a linear combination (Kurtz et al. 2015). This peak of 12.3 h can also be a subharmonic of the real rotation rate.

3.2.3. *G 226-29*

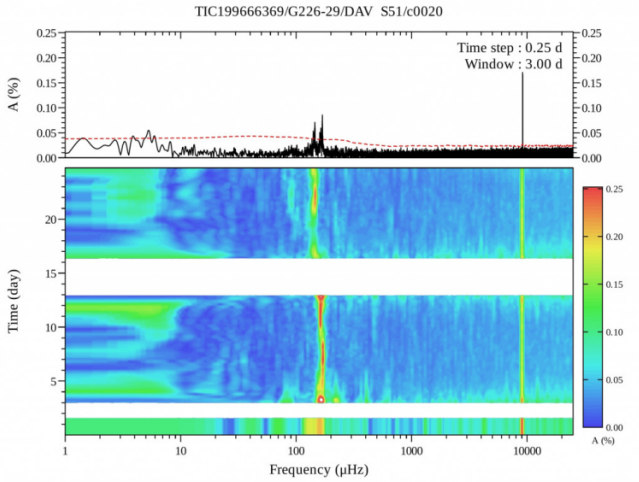

Figure 10. Running Fourier transform of G 226-29 20 s data from sector 51.

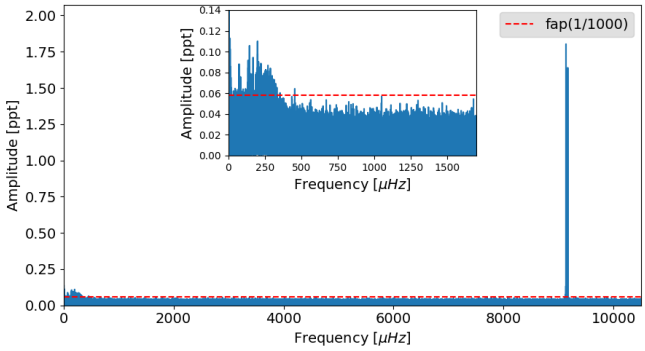

Figure 11. Fourier transform of G 226-29 20 s data from sectors 40 to 41 and 47 to 60. The inset plot zooms the FT at low frequencies. The red dashed line indicates the false alarm probability.

G 226-29 is the brightest known DAV, with a known pulsation triplet around 109 s (Kepler et al. 1983, 1995b). It was observed by TESS with 120 s exposures

in sectors 14 to 26, and 20 s exposures from sectors 40 to 41 and 47 to 60. Every sector shows an S/N$\simeq$ 4.1 wandering peak around 0.93 h (297.3μHz) to 3.25 h (85.5μHz) (see Figure sft), while the triplet, with periods 109.47243s@1.81mma, 109.27925s@0.53mma, and 109.08694s@1.64mma, shows a rotation period of 8.9 h (Kepler et al. 1995b). Figure 11 shows the FT of all 20 s data combined.

The methodology described in Section 1.1 assumes that the variability frequencies are constant. So, to verify if this wandering peak comes from G 226-29 star we had to apply the *TESS-Localize* test differently. For each sector, we got the highest peak exhibited in the FT ranging from 0.93 to 3.25 hours and ran *TESS-Localize* code for this period. As detailed in Table 3, *TESS-Localize* confirmed that this wandering peak comes from G 226-29.

4. GROUND-BASED OBSERVATIONS

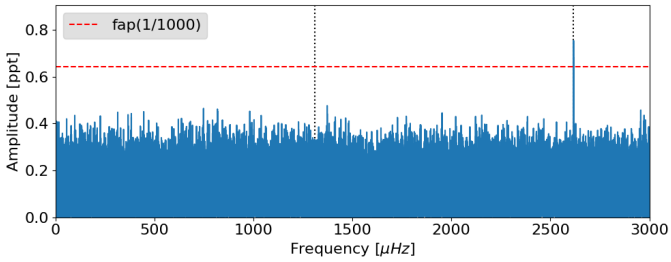

Figure 12. Fourier Transform of *TESS* data of star 'TIC 262548040'. The horizontal red line indicates the false alarm probability fap=1/1000 and the vertical dotted lines indicate the peak of 0.106 h and it's double.

Moss et al. (2023) obtained time-resolved spectroscopy for two magnetic WDs in our sample at Gemini Observatory. Based on the shifting positions of the Zeeman-split H_α components, they inferred a rotation period of 0.648 h for the star TIC 392797216 (LHS 2273). This period is very close to the 0.68 h period we found in the *TESS* data. Using the same method, they found that the star TIC 262548040 (LHS 1243) has a rotation period of 0.216 h. Figure 12 presents the FT of the data obtained by *TESS* for this star, showing that only one peak at 2617 μHz (0.106 h) is above the false alarm probability = 1/1000 (horizontal red line). The horizontal dotted lines indicate the peak of 0.106 h and it is double, showing that there is no significant peak at 0.212 h of the *TESS* data. Therefore, we can only detect the harmonic frequency in *TESS*, but the real rotation period is 0.212 h. Despite the harmonic issue, Moss et al. (2023) confirms the rotation rate for two of the fastest rotators in our sample.

5. EVOLUTIONARY MODELS

As we are studying the rotation rates of evolved white dwarf stars, assuming that the zero-age main-sequence models do not have differential rotation, one question that arises is how the evolution changes the internal velocities and how much of the initial angular momentum is lost during the expressive mass loss phase of AGB before the white dwarf phase.

5.1. *Observational and modeling context*

Using ground-based photometric observations time series from mean sequence stars spanning from late F to early M spectral types, Fritzewski et al. (2021) determined 279 rotation periods for members of the 300 Myr-old open cluster NGC 3532. They found that the rotation periods range from 0.5 d to 32 d, with trends of slow-rotating FGK stars and fast-rotating K dwarfs. In another recent investigation, Labadie-Bartz et al. (2023) explored the rotational characteristics of chemically peculiar (CP) stars located in the upper main sequence, utilizing *TESS* data. Among their findings is that the rotation period distribution of CP stars is centered around 3 days. CP stars are observed within the spectral types from early B to early F. Since all stars with spectral type roughly from A to K will become WDs, and we have demonstrated in this work that the median rotation period of WD is around 7 h, these findings suggest that a robust mechanism of internal angular momentum transfer operates during the evolution of the WDs progenitors.

Studying the internal rotation rates for hundreds of main-sequence stars in Gamma Doradus, Moyano et al. (2023) concluded that the transport of angular momentum in radiative zones during the main sequence of low-mass stars must be efficient, and the internal magnetic fields are a strong candidate for the missing physical ingredient in stellar interiors. In addition, they point out that at least one efficient process able to neutralize the development of differential rotation in stellar interiors must act during the whole evolution of this type of star.

Comparisons between models and asteroseismic determinations of core rotation rates for low- and intermediate-mass stars during evolved phases highlighted the need for varying efficiencies of internal angular momentum transport in different mass ranges to match observations (Moyano et al. 2022). Moyano et al. (2023) highlighted the importance of efficient angular momentum transport, possibly involving internal magnetic fields, throughout the main-sequence evolution of low-mass stars.

We computed evolutionary sequences using the Modules for Experiments in Stellar Astrophysics code (MESA,

Paxton et al. 2011, 2013, 2015, 2018, 2019; Jermyn et al. 2023), release 22.11.1. Our models have an initial mass of $M_{\rm i} = 1.5\ M_{\odot}$ and an initial metallicity of $Z = 0.02$, 0.002 and 0.001. The initial mass was chosen to be above the lower limit of 1.3 $M_{\odot}$ for the convective core in the main sequence (e.g. Aerts & Tkachenko 2023), leading to a white dwarf with mass close to the mean mass of most white dwarf stars (e.g. Kepler et al. 2007; O'Brien et al. 2023), and similar to the models of den Hartogh et al. (2019). They are computed from the zero-age main sequence (ZAMS) until a white dwarf cooling effective temperature of 8500 K. Our models start with equatorial surface rotation velocities of 10 and 50 km s^{-1}, typical of main-sequence stars with 1 and 2 solar masses. These values are assumed to be the solid-body rotations at the ZAMS. For further information on the models, see Appendix B - Evolutionary Models Input.

The mixing of elements and the transport of angular momentum due to rotation are implemented in MESA following closely Heger et al. (2000, 2005). Two efficiency factors must be set to calibrate the diffusion coefficients: the contribution of rotationally induced instabilities to the diffusion coefficient is reduced by the factor $f_{\rm c} = 1/30$, and the sensitivity of rotationally induced mixing is $f_{\mu} = 0.05$.

We consider the following angular momentum transport mechanisms: Dynamical shear instability, Solberg-Hoiland, secular shear instability, Eddington-Sweet circulation, Goldreich-Schubert-Fricke and the Spruit-Tayler dynamo.

The final masses of our models are 0.546 $M_{\odot}$ for $Z = 0.02$, 0.577 $M_{\odot}$ for $Z = 0.002$, and 0.585 $M_{\odot}$ for $Z = 0.001$. This aligns with expectations that stars with higher metallicity should form less massive CO cores and therefore lower final masses, and lose more mass in the AGB phase than stars with the same initial mass but lower metallicity (e.g., Dominguez et al. 1999; Catalán et al. 2008; Romero et al. 2015; Choi et al. 2016). Similar models with initial masses of 2.5 $M_{\odot}$ reach the white dwarf phase with masses around 0.6 $M_{\odot}$.

In Figure 13 we show the evolution of the surface rotational period (P) versus the effective temperature ($T_{\rm eff}$) during the cooling track for a set of model sequences with different metallicity and initial rotation velocity. The surface rotational period is computed via $P = 2\pi r/v$, where r is the model radius and v is the rotational velocity at the equator. Sequences that consider the six mechanisms of angular momentum transport are shown as dotted lines (AMT=ON), and the solid lines represent sequences with all the mechanisms turned off (AMT=OFF).

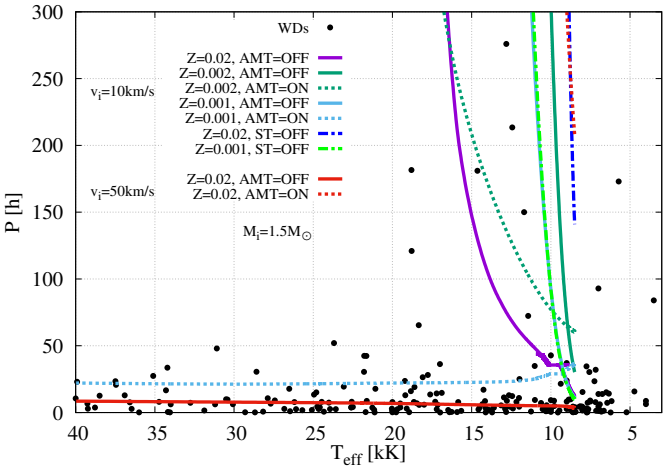

Figure 13. Observational data of the surface rotation of white dwarf stars (black dots) are compared against evolutionary models showing the rotation period in the white dwarf cooling track. We compare models with the six mechanisms of angular momentum transport turned off (solid lines) and on (dotted lines) during the whole evolution. For initial rotational velocity of $v_{\rm i} = 10$ km s^{-1}, we present models with metallicities of $Z = 0.02$ (purple), 0.002 (dark green), and 0.001 (light blue). We also compare two models where the Spruit-Tayler dynamo is the only mechanism turned off during the computations (dark blue and light green dotted-dashed lines). For an initial rotational velocity of $v_{\rm i} = 50$ km s^{-1}, we compare two models with $Z = 0.02$ (red lines). All model sequences have an initial mass of 1.5 M$_{\odot}$.

For $v_{\rm i} = 10$ km s^{-1} and $Z = 0.02$ (purple line in Figure 13), we find that the models with AMT = OFF decrease the average equatorial rotation period on the surface from $P = 300$ h to ~ 30 h when cooling from ~ 17 kK to 8500 K. The sequence with AMT=ON does not even reach 300 h before cooling down to the same temperature (and therefore does not appear in the plot).

For sequences with $Z = 0.002$ (dark green lines in Figure 13), we find that if AMT=OFF (solid line), the models brake from $P = 300$ h to 40 h only at the very end of the cooling track ($T_{\rm eff} < 10$ kK), while the AMT=ON sequence (dotted line) has already spun down to 300 h when $T_{\rm eff} < 17$ kK, although it reaches only $P \sim 60$ h at $T_{\rm eff} = 8500$ K.

The internal redistribution of the angular momentum is very efficient early in the evolution of low-mass stars (e.g., Mosser et al. 2012). This suggests that when AMT=ON, a large amount of mass lost by winds during the AGB phase carries away most of the angular momentum, and thus, the surfaces of the models rotate slower in the WD phase.

The difference in turning the angular momentum transport mechanisms on and off is much more pronounced for low metallicity. ($Z = 0.001$, light blue in

Figure 13). While AMT=OFF (solid line) follows the same trend as for higher metallicities (that is, reaching low P only at the end of the cooling track), the sequence with AMT=ON (dotted line) cools from $T_{\rm eff}$ = 40,000 K down to 8500 K with approximately constant rotation period of P = 25 h, closer to most of the observed period distribution.

In Figure 13 we also show two sequences of models with $v_{\rm i}$ = 10 km s^{-1} where the Spruit-Tayler mechanism was turned off, and all the other five mechanisms were kept on during the whole evolution (ST=OFF, dotted-dashed lines). For Z = 0.001 (light green line), the result is similar to that of the same metallicity, but with all six angular momentum transport mechanisms turned off. This suggests that the Spruit-Tayler mechanism dominates over the other mechanisms from the point of view of the rotation analysis during the WD phase.

Finally, we present two sequences with $v_{\rm i}$ = 50 km s^{-1} and Z = 0.02. These models show that observational data with a shorter rotation period (P < 50 h) are better adjusted by models with AMT=OFF, while models with AMT=ON present a rotation period shorter than 300 h only at the end of white dwarf cooling when $T_{\rm eff}$ < 10 000 K. This suggests that if we disregard the Spruit-Tayler mechanism throughout the evolution, models with a higher initial velocity (50 km s^{-1}) fit the white dwarf rotation data better if the initial mass is 1.5 M$_{\odot}$.

6. CONCLUSION

Assuming that the variability detected in the *TESS* data is caused by rotation, Table 1 shows that, independent of the applied selection thresholds, the most probable rotational period of WDs is about 7 h. The right panels of Figure 5 show that, for all samples, more than 60% of the stars present periods shorter than approximately 10 h. The stricter the sample, the more prominent the distribution of the rotational periods of the WD around three different values: approximately 3 h, 8 h, and 24 h. This result agrees with the distribution of rotational periods from seismology, which also presents a similar pattern. Detecting periods shorter than approximately 12.5 h through seismology are less frequent than our findings. Consequently, the seismological sample shows a higher median rotational period of 27 h and a standard deviation of 30 h. For the ground observations, there is a selection bias that observations last in general 3 to 4 h, limiting the frequency resolution. The similarity of the period distribution of our samples and the seismological period distribution is a good indicator that our samples represent the rotation rate of the WDs. The figures presented in Section 2 also indicate that binary WDs do not exhibit a preferential mass, temperature, or period. However, despite the small sample, magnetic WDs are preferentially massive, cool, and fast rotators.

Sample 1 presents a median effective temperature of 18800 K and a median mass of $0.51 M_{\odot}$. As discussed in Section 2.1, Figure 2 could indicate a large concentration of WDs formed in interacting binary systems, despite observational bias. However, this does not mean that these stars are still in binary systems, nor that detected variability comes from orbital motion. Figure 2 also shows that short periods (shorter than 10 h) are not restricted to low-mass WDs; instead, they are distributed throughout the mass range. Even if we assume that all WDs in our sample with a mass less than $0.45 M_{\odot}$ are in binary systems and that the variabilities detected are due to ellipsoidal variation, it does not change our findings. Figure 6 shows that the rotation period histogram that excludes low-mass WDs remains the same: periods shorter than 10 h are by far the most common. Therefore, this figure reaffirms that the hundred short rotation period stars we detect are not related to the large concentration of low-mass WDs in our sample.

Moss et al. (2023) confirmed the rotation period we detected in *TESS* data for two of the fastest rotators in our sample. Using ground-based observations, they detected rotation periods very close to our findings but also provided an example of half-period aliases. For TIC 262548040, we only detect in *TESS data* the harmonic of the real rotation period. Without the ground-based observations of Moss et al. (2023), we would not be able to know that the signal we detected was of a harmonic frequency. Therefore, we may be detecting and reporting half of the real rotation period for other stars. However, it does not invalidate our findings, since the same work confirmed rotation periods of 0.68 h and 0.21 h for two magnetic WDs in our sample.

We detected non-pulsating periods for 3 of WDs with rotation period determined through asteroseismology. For NGC 1501, we detected periods of 4.11, 39, and 138 hours. This pre-white dwarf is the central star of a planetary nebula, that is, a complex system. Therefore we are not able to interpret any of these periods. The star 'TIC 7675859' presents a triplet in the *TESS* data. Using its frequency spacing, we determined the seismological rotation period of this star as 6.34 hours. However, its FT also presents a significant period of 12.3 hours. Although the amplitude of this period is higher than the amplitude of all components of the triplet, we do not discard the possibility of a linear combination. We also consider the possibility of the 12.3 h period being a subharmonic or even the photometric rotation

period itself. We found that the WD G 226-29 exhibits a wandering peak varying from 0.93 to 3.25 hours. Its seismological rotation period is much longer than these values, 8.9 h.

For 5 of the 266 WDs in our sample, the variabilities detected in *TESS* data were also reported by Farihi et al. (2023). They are TIC 328029653, TIC 251080865, TIC 251903434, TIC 204440456 and TIC 321979116. The reported periods agree with our findings. They claim that the variability found in the WD 2138-332 data (TIC 204440456) is the stellar rotation period, almost certainly due to magnetism.

Most of the stars in our sample that exhibit rotation periods shorter than 50 h present an effective temperature lower than 40 kK. Figure 13 presents two models that at 40 kK reach rotation periods consistent with the findings of this work. We find that periods shorter than 50 h and are well-fitted by models with $Z = 0.02$, $v_{\rm i} = 50$ km s^{-1} and angular momentum transport set to OFF; or by models with $Z = 0.001$, $v_{\rm i} = 10$ km s^{-1} and angular momentum transport set to ON. A smaller part of the observational data presents a large dispersion of the rotation period and is concentrated at $T_{\rm eff} < 20{,}000$ K. Our remaining models best fit these stars.

While other studies have shown that the internal transfer of angular momentum should be intense in the early phase of the evolution of low-mass stars, our study confirms that if we seek to match most of the white dwarf rotational data, this redistribution should cease or be less intense before the end of the AGB phase, when stars lose the highest amount of mass and, therefore, angular momentum. If we assume that stars with lower metallicity will have a lower mass loss rate due to winds at the top of the AGB phase (e.g., see discussion in Höfner & Olofsson 2018), this means that they will lose less angular momentum and therefore rotate faster in the WD phase. However, when we consider that more angular momentum transfer mechanisms have been activated since the beginning of the evolution, more angular momentum will be transferred to the surface and lost during the AGB phase. Thus, in terms of the WD rotation period, lowering the metallicity is equivalent to reducing the angular momentum transfer mechanisms in the early evolution. Due to their intrinsic faintness, the observed white dwarfs are mainly nearby galactic disk objects, most likely with metallicity closer to the Sun's.

In general, our models agree with the most recent results in the literature in the sense that different initial parameters can be used to create models that are in agreement with a particular part of the observational data, but there is a degeneration in the parameter space (i.e., the initial velocity of rotation, initial mass, metallicity, etc.) that could be better resolved if we knew more precisely how the redistribution of angular momentum occurs in stellar interiors.

In the future, we will analyze *TESS* data observed after Oct. 2023, calculate models with the Fuller dynamo prescription, and extend the mass range of the models as the data include white dwarfs with a range of masses.

This work was carried out with the financial support of the Conselho Nacional de Desenvolvimento Científico e Tecnológico (CNPq), and by the Coordenação de Aperfeiçoamento de Pessoal de Nível Superior - Brasil (CAPES). We thank Stephan Charpinet for providing the running Fourier Transform of the star G 226-29. This research has made extensive use of NASA's Astrophysics Data System Bibliographic Service (ADS), SIMBAD, and MAST. We used ASTROPY (https://www.astropy.org/), TESS-LS (https://github.com/ipelisoli/TESS-LS), TESS-LOCALIZE (https://github.com/Higgins00/TESS-Localizer), lightkurve (https://docs.lightkurve.org/), PYRIOD (https://github.com/keatonb/Pyriod).

APPENDIX

APPENDIX A - KNOWN RR LYRAE STAR

BPM 24754 (TIC 367227831) is a knownvariable white dwarf. Figure 14 shows its FT of *TESS* data plotted using the Pyriod software (Bell 2020). In this case, we know that the primary signal at 21.49μ Hz (12.92 h) and its harmonics are the contamination from the known RR Lyrae variable *Gaia DR3 5923100101270979328* (TIC 367227833). The results of software *TESS-Localize* for the three sectors where the star is observed (12, 39, and 66) are:

TESS-Localize estimates that the probability that the signal source is the RR Lyra star is 75% in sector 12, even the parameters *pvalue* and *Height* indicating good values. The *Relative Likelihood* of the RR Lyrae star being the source of signal increases in the subsequent sectors, with the mean like reaching 85%. The second source is likely the same for all three sectors, *Gaia DR3 5923100101249048320*. This object is located 3.06*arcsec* away from the RR Lyrae star.

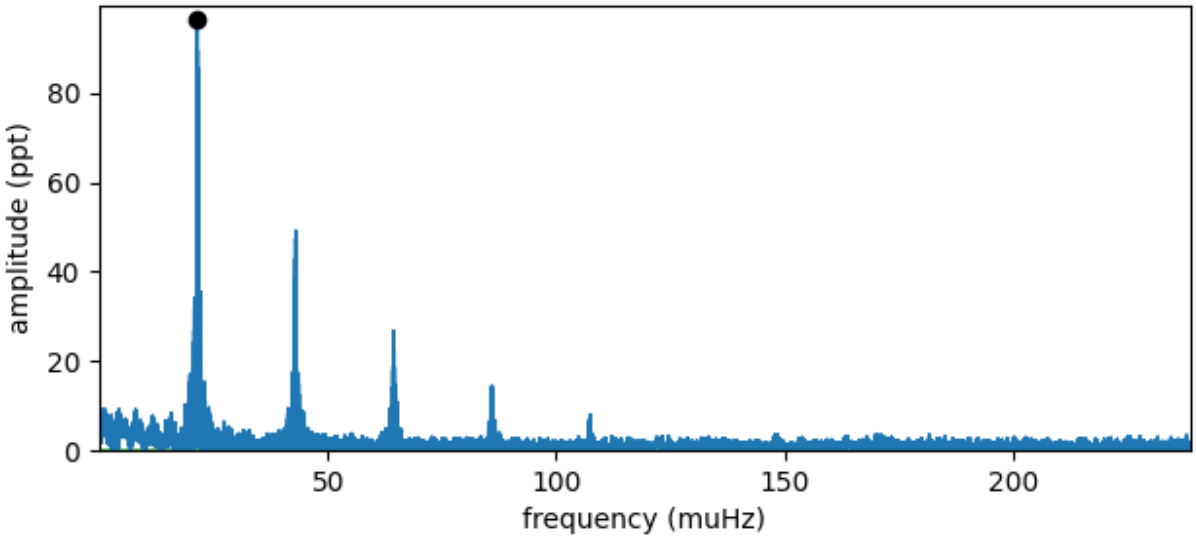

Figure 14. BPM 24754 light curve from sectors 12, 39, and 66.

Sector	Source	pvalue	Relative Likelihood	χ^2	*Height* [σ]
12	'5923100101270979328'	0.214	0.75	44.40	42.40
12	'5923100101249048320'	0.071	0.19	44.40	42.40
39	'5923100101270979328'	0.503	0.83	312.71	17.30
39	'5923100101249048320'	0.191	0.11	312.71	17.30
66	'5923100101270979328'	0.829	0.96	62.47	37.22
66	'5923100101249048320'	0.198	0.03	62.47	37.22

Table 4. *TESS-Localize* results to the signal 12.92 h in present in the light curve of teh DAV BPM 24754.

APPENDIX B - EVOLUTIONARY MODELS INPUT

Hydrogen and helium burning are computed using the `pp_and_cno_extras.net` network that accounts for 25 isotopes and 79 net reactions. Convection is treated using the formulation of the mixing−length theory (Böhm-Vitense 1958) in the variation of Henyey et al. (1965) allowing the convective efficiency to vary with the opacity. We set the diffusion of elements for the whole net; each isotope in the network is treated as its own class.

Following the MIST project (Choi et al. 2016), $\alpha_{\rm MLT} = 1.82$ is adopted as the mixing length parameter. We consider the Ledoux criterion of stability, which considers the influence of composition gradients on mixing. Semiconvection is considered unstable regions by the Schwarzschild criterion, but stable by Ledoux, with an efficiency parameter $\alpha_{\rm sc} = 0.1$. Thermohaline mixing is included throughout evolution, with efficiency $\alpha_{\rm th} = 666$.

Exponential overshooting is set to $f = 0.008$ in the core and 0.0087 in the shell. We handle mixing in the convective zones using the convective premixing scheme. For the boundary conditions of the atmosphere, we use the $T(\tau)$ Eddington relation with varying opacity for most of the evolution and hydrogen atmosphere tables for cool white dwarfs (Rohrmann et al. 2011) when the models are on the cooling track and the effective temperature is below 10,000 K. The mass loss by stellar winds is taken into account using the Reimers (1975) scheme with $\eta_{\rm R} = 0.5$ for the red giant branch phase and the Bloecker (1995) scheme with $\eta_{\rm B}$ varying between 0.1 and 1 for the asymptotic giant branch phase.

APPENDIX C - ROTATIONAL PERIODS TABLE

Table 5. Photometric rotation Periods.

TIC	Period [h]	Amplitude [σ]	Like	$\langle$ Height [σ] $\rangle$	$T_{\rm eff}$ [K]	Mass [$M_\odot$]	Q/S	info
144002497	7.6213 ± 0.0022	48.042	1.00	42.8	72910	0.606	2/2	
837076117	11.468 ± 0.007	7.899	1.00	11.2	81335	0.65	1/2	DA
307982318	1.53006 ± 7e-05	4.803	1.00	5.0	31880	0.67	1/3	hotDAV
88564975	8.9702 ± 0.003	173.775	1.00	92.9	80000	0.67	3/3	
136884288	0.6053 ± 0.0006	7.730	1.00	13.6	8440	0.81	1/1	DAHe
383647517	13.924 ± 0.014	13.263	1.00	6.2	6754	0.545	7/16	DQpec
1102584065	26.187 ± 0.022	17.910	1.00	9.1	110000	0.57	12/13	DO
436747174	4.166 ± 0.026	290.193	1.00	59.7	22500	0.532	1/1	DA-CV
434196824	3.904 ± 0.023	53.066	1.00	62.4	14491	0.258	1/1	
345265261	3.759 ± 0.022	7.601	1.00	12.2	38780	0.843	1/1	DA
321272216	4.408 ± 0.031	34.385	0.99	40.0	12597	0.117	1/1	
248861930	12.93 ± 0.26	23.353	1.00	28.0	36903	0.521	1/1	DBA
247992671	15.4 ± 0.4	8.742	1.00	10.8	8000	0.23	1/1	
241256067	15.778 ± 0.028	5.352	1.00	6.0	4730	0.495	1/2	DC
124894242	0.32555 ± 0.00017	4.075	1.00	6.9	15919	0.435	1/1	
154942231	4.4236 ± 0.0022	7.839	1.00	6.4	12000	0.15	3/5	
649932200	0.9712 ± 0.0005	31.107	1.00	28.4	26461	1.036	3/3	
52584399	3.801 ± 0.008	112.873	1.00	66.8	19505	0.249	3/3	
1883129777	1.9446 ± 0.0004	143.936	1.00	71.9	16480	0.229	3/3	
1881564044	6.137 ± 0.004	6.042	1.00	7.4	34000	0.2	2/3	DAH
1101460688	23.24 ± 0.03	10.905	1.00	6.9	88000	0.656	2/3	
22014729	7.6477 ± 0.0032	135.408	1.00	55.8	36580	0.44	1/2	
31798074	21.828 ± 0.017	42.369	1.00	5.3	12011	0.398	1/10	
262921847	13.892 ± 0.004	52.290	1.00	20.7	7000	0.23	12/12	
311886800	10.2157 ± 0.0025	32.576	1.00	19.4	100000	0.6	6/6	
178994042	0.2138 ± 7e-05	4.400	1.00	5.6	19770	0.57	1/1	
220478684	16.611 ± 0.010	25.143	1.00	12.6	44589	0.483	19/20	
381976323	8.722 ± 0.01	133.547	1.00	45.2	4000	0.2	11/11	
235072034	84.0 ± 4.0	20.540	1.00	10.5	3500	0.23	2/3	
219244444	7.2886 ± 0.0027	245.106	1.00	12.5	6440	0.25	3/5	DA7+M+planet
245834374	33.6 ± 1.8	7.275	1.00	6.8	34210	0.69	1/1	DA+M
85146644	5.317 ± 0.0011	68.977	1.00	51.4	60260	0.41	3/3	
107310223	11.28 ± 0.23	21.505	1.00	30.9	48116	0.366	1/1	DA1+dM
1101900758	2.65191 ± 0.0003	31.335	1.00	21.4	23941	0.398	5/5	
160119816	21.453 ± 0.017	112.794	1.00	43.3	90000	0.56	9/9	
300284179	12.65 ± 0.29	12.426	1.00	13.8	38490	0.54	1/1	
126910998	19.4 ± 0.6	36.753	1.00	54.9	23075	0.819	1/1	DA+M
218971976	6.7081 ± 0.001	263.431	1.00	65.1	39260	0.38	2/2	DA+M
321979116	2.69506 ± 0.00016	92.402	1.00	36.5	8650	0.96	2/2	DAP5.8
183533908	2.55267 ± 0.00024	11.122	1.00	13.6	7638	0.74	1/1	
630539472	1.592 ± 0.004	4.231	1.00	7.4	10027	0.821	1/1	
201255204	6.34 ± 0.03	59.895	1.00	52.0	4000	0.2	2/2	DBH
439917321	12.98 ± 0.28	61.269	1.00	48.6	19193	0.57	1/1	DA+M
55096188	2.75096 ± 0.00021	4.379	1.00	6.5	10000	0.6	2/3	
53190694	9.923 ± 0.004	12.529	1.00	9.3	30502	0.41	3/4	DA3+dM
952264940	1.78894 ± 0.00018	7.713	1.00	8.6	25692	1.151	1/2	DBH

TIC	Period [h]	Amplitude [σ]	Like	$\langle$ Height [σ] $\rangle$	$T_{\rm eff}$ [K]	Mass [$M_\odot$]		info
219769847	8.72 ± 0.13	13.789	1.00	20.7	21620	0.72	1/1	DA3+dM
292114384	0.29255 ± 0.00014	4.110	1.00	5.1	18943	0.57	1/1	
66714896	12.579 ± 0.009	10.848	1.00	8.8	63073	0.69	1/3	
349233389	52.0 ± 5.0	31.595	1.00	25.7	23690	0.58	1/1	DA2+M
335501964	6.7654 ± 0.0025	5.380	1.00	8.1	90000	0.53	1/2	
165916724	0.092325 ± 5e-07	4.156	1.00	5.2	9557	0.883	1/3	DAH
274039489	7.32 ± 0.09	67.842	1.00	58.5	42370	0.66	1/1	DA1.2+binary
328029653	14.157 ± 0.004	19.335	0.99	12.5	6340	0.53	5/5	
311920919	0.1614889 ± 1e-06	4.611	1.00	6.2	14116	0.68	1/4	
155871645	0.1385659 ± 8e-07	6.552	1.00	5.5	34050	0.77	3/5	
344927121	2.53418 ± 0.00018	113.339	1.00	67.3	26088	0.381	4/4	
148719841	8.549 ± 0.004	17.920	1.00	18.7	6169	0.72	2/2	
397535923	0.206167 ± 1.6e-05	4.293	1.00	5.2	5222	0.537	1/2	
415714190	0.384926 ± 4e-06	9.333	1.00	8.4	7690	0.636	3/3	
277713491	8.9986 ± 0.0032	11.795	1.00	9.2	7518	0.578	3/4	
471013515	6.05 ± 0.07	27.262	1.00	34.8	55000	0.6	1/1	
5393020	1.5786 ± 0.00014	54.426	1.00	49.4	8000	0.35	1/2	
610754879	0.91146 ± 9e-05	11.175	1.00	10.9	47617	1.341	2/3	
365207316	2.539 ± 0.005	6.316	1.00	7.1	10520	0.226	2/2	
425079955	17.076 ± 0.016	20.821	1.00	16.2	14252	0.285	2/2	
1271382181	7.426 ± 0.005	40.083	1.00	21.8	24015	0.25	8/8	
115970839	2.6994 ± 0.0004	41.932	1.00	30.0	8825	0.219	5/5	DA+M:
159819681	10.728 ± 0.006	29.967	1.00	22.8	27876	0.573	5/5	
158971558	6.327 ± 0.004	7.300	1.00	7.3	14319	0.323	2/2	
1550807820	0.566897 ± 1.6e-05	5.636	1.00	8.6	44523	1.293	5/5	
7622101	8.5708 ± 0.0028	11.742	1.00	7.6	14159	0.2	7/7	
349993999	4.381 ± 0.0005	7.642	1.00	7.0	24751	0.756	1/1	
1688534307	0.0902002 ± 4e-07	4.253	1.00	5.3	66522	0.637	1/2	
62918265	4.6612 ± 0.0008	12.845	0.99	13.1	8133	0.724	6/6	
1922433415	2.03387 ± 0.00015	129.416	1.00	60.4	21155	0.214	2/2	
100469915	12.936 ± 0.006	18.310	1.00	21.6	12644	0.152	2/2	
2026050241	8.0844 ± 0.0024	6.393	1.00	5.7	48831	0.489	1/2	
60112260	7.37 ± 0.1	14.436	1.00	20.0	7682	0.756	1/1	
269937578	7.2969 ± 0.0019	79.671	1.00	45.4	32755	0.274	4/5	
2052430471	0.125404 ± 2.9e-05	4.277	1.00	5.4	28678	0.368	1/1	
124573902	7.9918 ± 0.0035	21.546	1.00	21.9	12173	0.371	2/2	eclipse
270432557	9.311 ± 0.01	6.316	1.00	5.4	10000	0.23	2/3	
43529091	9.44 ± 0.14	11.479	1.00	14.0	11006	0.17	1/1	
278861557	3.1624 ± 0.0004	26.520	1.00	7.8	10460	0.23	19/20	binary
62846288	0.500906 ± 1.4e-05	23.831	1.00	17.9	16268	0.935	3/4	
56813164	8.05 ± 0.11	25.988	1.00	34.7	17304	0.39	1/1	DA+M
953086708	0.088138 ± 1.3e-05	5.293	1.00	7.4	7735	0.564	1/1	DAEH
95475692	1.94319 ± 0.00021	45.117	1.00	36.2	13737	0.428	2/2	DA+M
68015843	3.015 ± 0.0018	21.609	1.00	21.7	12392	0.4	2/2	DA+M4.5
219485299	1.9770 ± 0.0020	4.513	1.00	18.9	10307	0.63	3/3	DA+M
1507548590	1.9272 ± 0.0004	50.124	1.00	49.2	25089	0.214	2/2	
1101327387	1.30545 ± 9e-05	21.739	1.00	19.5	15659	1.13	2/2	DAH
416538823	16.021 ± 0.011	335.044	1.00	26.1	18840	0.8	4/4	DA+M

TIC	Period [h]	Amplitude [σ]	Like	$\langle$ Height [σ] $\rangle$	$T_{\rm eff}$ [K]	Mass [$M_\odot$]		info
7983187	14.32 ± 0.16	77.693	1.00	45.2	17210	0.59	2/2	DA3+dM
251857373	2.31675 ± 0.00012	175.807	1.00	110.6	40698	0.56	2/2	
408015814	29.52 ± 0.05	13.089	1.00	11.8	76010	0.061	2/2	
200725303	9.48 ± 0.07	35.024	1.00	33.5	90000	0.75	2/2	
159894126	0.46415 ± 0.00017	4.410	1.00	5.9	8627	0.613	1/2	
651923454	42.4 ± 2.9	16.656	1.00	11.9	21644	0.746	1/1	binary
651337335	30.5 ± 1.5	6.331	1.00	9.7	21796	0.217	1/1	
650999219	24.6 ± 0.5	24.641	1.00	26.3	70000	0.49	2/2	
93031595	9.94 ± 0.16	17.306	1.00	25.7	8751	0.911	1/1	DZ
685012668	2.8735 ± 0.0018	107.688	1.00	44.9	20041	0.238	5/5	
672383331	17.8 ± 0.5	7.107	1.00	10.9	21076	0.279	1/1	
257689590	13.35 ± 0.13	5.132	0.99	5.2	8629	0.183	2/2	
455072135	11.36 ± 0.21	90.850	1.00	49.0	12965	0.116	1/1	EB
941411508	10.547 ± 0.006	8.630	1.00	9.1	40000	0.556	2/2	
942842236	8.233 ± 0.004	10.210	1.00	10.1	77164	0.75	2/2	
332828037	2.07518 ± 0.00024	15.973	1.00	17.4	13936	0.382	2/2	
939953390	29.85 ± 0.05	9.949	1.00	6.7	63208	0.667	3/3	
952000432	21.158 ± 0.025	23.145	1.00	23.4	81500	0.58	2/2	
232524621	3.4918 ± 0.0005	14.341	1.00	8.5	100000	0.65	2/9	hotDA+binary
1003414425	26.46 ± 0.04	25.074	1.00	16.5	18089	0.173	4/4	
233177285	15.194 ± 0.01	4.790	1.00	6.2	6500	0.2	2/6	
232979174	8.8045 ± 0.0033	8.642	1.00	5.6	12776	0.473	2/9	
1001602651	4.9125 ± 0.0018	10.704	1.00	7.2	9786	0.826	5/6	
219009693	1.5828 ± 0.0004	9.973	1.00	7.3	14000	0.23	4/4	
364160098	0.19744 ± 6e-05	4.307	1.00	5.7	20000	0.2	1/1	
471013541	0.549 ± 0.0005	4.071	1.00	5.6	88642	0.51	1/1	
951282189	2.9618 ± 0.0005	95.469	0.99	110.8	19099	0.174	2/2	DAB+binary
951635495	23.45 ± 0.03	7.002	1.00	6.6	61045	0.5	2/2	
1924161836	25.132 ± 0.024	14.278	1.00	12.4	71080	0.482	2/2	
410414842	14.9 ± 0.4	6.417	1.00	9.7	70000	0.5	1/1	
2052284133	16.652 ± 0.03	12.980	1.00	14.3	34299	0.51	2/2	
251080865	32.01 ± 0.06	179.265	1.00	38.0	7170	0.744	2/2	DCP7
164681986	3.9437 ± 0.0009	33.642	1.00	31.3	8471	1.006	2/2	
392797216	0.6808 ± 0.0004	6.037	1.00	6.0	6814	0.749	2/2	DAH
157201137	0.776229 ± 3.3e-05	10.198	1.00	10.9	11254	0.486	2/2	CV
219868627	5.9071 ± 0.0017	43.787	1.00	18.3	18000	0.18	12/12	DAZ+binary
155872634	3.9145 ± 0.0007	26.280	1.00	16.7	24589	0.697	6/6	
357389336	42.46 ± 0.08	7.007	1.00	6.1	21785	0.49	2/5	DA+K
313894558	19.05 ± 0.04	4.861	0.99	5.2	18610	0.61	1/2	
441569276	2.47353 ± 0.00023	90.759	1.00	55.4	19690	0.43	6/6	DA+M
457099062	1.36615 ± 0.0002	7.658	1.00	8.2	6655	0.555	2/2	
198510602	8.87 ± 0.013	110.918	1.00	46.3	9800	0.23	4/4	
236865474	17.789 ± 0.011	55.795	1.00	21.0	26520	0.52	14/14	DA1.9+binary
279484490	0.086195 ± 1.2e-05	4.519	1.00	5.8	16989	0.387	1/1	
248353420	11.32 ± 0.26	105.385	1.00	69.0	60419	0.53	1/1	DA+K
54003343	22.864 ± 0.029	16.612	1.00	18.5	52869	0.611	1/2	DA1+dM
71513592	23.0 ± 0.9	11.500	1.00	15.8	39910	0.438	1/1	
737660462	9.703 ± 0.013	30.331	1.00	23.7	30415	0.502	5/5	

TIC	Period [h]	Amplitude [σ]	Like	$\langle$ Height [σ] $\rangle$	$T_{\rm eff}$ [K]	Mass [$M_\odot$]		info
60040774	9.72 ± 0.15	9.104	1.00	14.7	8876	0.277	1/1	eclipse
712210226	0.115822 ± 2.2e-05	4.178	1.00	5.5	13707	0.53	1/1	binary
705867935	0.28689 ± 0.00013	6.605	1.00	13.7	16407	1.001	1/1	
765410943	3.7702 ± 0.0005	169.012	1.00	55.6	22601	0.238	19/19	
96391732	3.662 ± 0.011	98.438	1.00	117.0	21272	0.183	2/2	
291303146	14.36 ± 0.33	43.492	1.00	40.9	100000	0.58	1/1	
770913638	0.453289 ± 1.1e-05	19.139	1.00	21.2	8474	0.794	2/2	
743328948	7.9 ± 0.1	28.663	1.00	45.6	20000	0.2	1/1	
403672198	3.137 ± 0.016	25.892	1.00	38.6	7750	0.23	1/1	
437213912	37.1 ± 2.3	29.331	1.00	34.2	9000	0.2	1/1	
836046041	7.9019 ± 0.0034	12.734	1.00	15.5	26187	0.517	2/2	
817911025	0.597463 ± 1.9e-05	17.981	1.00	16.0	84000	0.63	3/4	
832516183	30.55 ± 0.05	9.190	1.00	9.2	28583	0.403	1/1	
804549027	2.948 ± 0.007	117.121	1.00	79.0	10000	0.2	2/2	
191532802	3.553 ± 0.022	5.513	1.00	11.6	8630	0.808	1/1	
262708252	5.4411 ± 0.0015	28.747	1.00	16.1	10266	0.152	7/7	
841325183	2.504 ± 0.0005	10.370	1.00	9.2	17205	0.28	3/4	
873285117	20.79 ± 0.024	9.782	1.00	9.9	37453	0.349	1/2	
875311151	11.053 ± 0.007	9.792	1.00	8.7	50475	0.491	1/2	
309025727	8.22 ± 0.06	19.948	1.00	26.6	9000	0.23	1/2	
870310469	23.443 ± 0.03	9.701	1.00	9.9	37491	0.502	2/2	
841399917	36.32 ± 0.15	64.304	1.00	39.3	17000	0.2	4/4	
33357141	13.47 ± 0.31	8.387	1.00	11.5	24952	0.526	1/1	
345036441	1.64579 ± 8e-05	13.629	1.00	10.6	10355	0.92	4/5	DAH
471013677	2.79285 ± 0.00031	59.858	1.00	53.6	36470	0.6	1/4	
902670676	22.988 ± 0.029	10.934	1.00	10.8	78000	0.66	2/2	
82347011	6.2108 ± 0.0021	130.009	1.00	94.0	30071	0.4	2/2	DA+M3
950218375	10.3 ± 0.19	7.101	1.00	10.0	42180	0.52	1/1	
232972481	81.13 ± 0.28	89.769	1.00	39.0	99575	0.87	7/7	DA+M
156073827	0.189861 ± 2e-06	10.486	1.00	10.0	29300	0.415	2/3	
115613388	0.703919 ± 2.6e-05	6.117	1.00	5.3	28169	1.272	2/5	DAH
630123582	4.109 ± 0.027	3.846	1.00	12.5	60000	0.456	1/1	
630314437	0.17219 ± 5e-05	4.425	1.00	6.9	21128	0.526	1/1	binary
399570361	10.89 ± 0.22	25.327	0.99	27.6	79000	0.656	1/1	binary
183799565	0.689793 ± 2.6e-05	5.825	1.00	5.8	180000	0.54	1/4	
142982488	0.40188 ± 0.00026	4.112	1.00	5.6	34180	0.626	1/1	
298411553	2.90014 ± 0.00031	12.166	1.00	8.2	39229	0.756	4/8	
80858168	2.84122 ± 0.0003	38.679	1.00	34.0	12891	0.256	3/3	
652008669	48.0 ± 4.0	6.901	1.00	6.0	31092	0.432	1/1	
412252434	2.40744 ± 0.00022	7.758	1.00	12.8	10206	0.597	4/4	
760481896	6.641 ± 0.005	64.546	1.00	32.8	27691	0.404	4/4	
453006983	9.093 ± 0.005	19.789	1.00	21.5	27425	0.52	2/2	DA+M
804378446	29.44 ± 0.05	12.366	1.00	14.6	48986	0.685	2/2	
310478036	2.36875 ± 0.00029	11.001	1.00	59.3	7000	0.23	7/7	
349408306	3.6493 ± 0.0005	84.357	1.00	25.5	8000	0.15	21/21	
462519068	4.987 ± 0.008	4.490	1.00	19.7	7000	0.15	3/3	
119736060	3.954 ± 0.026	49.116	1.00	56.6	22600	0.42	1/1	DA+M
46199750	1.891 ± 0.008	7.440	1.00	13.9	20000	0.94	1/1	DAP

TIC	Period [h]	Amplitude [σ]	Like	$\langle$ Height [σ] $\rangle$	$T_{\rm eff}$ [K]	Mass [$M_\odot$]		info
147918835	2.722 ± 0.012	156.826	1.00	63.5	24661	0.21	1/1	
142808656	7.9038 ± 0.0034	11.463	1.00	10.0	18646	0.031	4/4	
258086867	30.3 ± 1.5	7.607	1.00	5.6	7573	0.753	1/1	
1000946479	2.69774 ± 0.00032	4.572	1.00	5.8	7139	0.6	1/4	DC
274928438	2.464 ± 0.01	5.552	1.00	6.6	6959	0.23	1/1	DA+M
1100582330	2.736 ± 0.017	18.131	1.00	29.2	26828	0.496	1/1	
284900652	7.9923 ± 0.0021	359.311	1.00	71.7	34733	0.36	29/29	DA+dMe
383673264	72.37 ± 0.17	15.671	1.00	6.8	11435	0.661	11/25	
25771075	7.8738 ± 0.0023	14.170	1.00	14.5	15849	0.263	3/3	
47499442	7.83 ± 0.1	18.473	1.00	22.7	7184	0.562	1/1	
33692053	15.1 ± 0.4	14.656	1.00	20.4	24809	0.239	1/1	
34855316	4.461 ± 0.032	30.907	1.00	46.5	8021	0.745	1/1	
355154138	2.37013 ± 0.00029	18.259	1.00	11.4	14569	0.403	7/7	
429233827	7.17 ± 0.0028	113.682	1.00	74.9	10618	0.174	2/2	
32159409	42.8 ± 3.2	9.008	1.00	11.7	10000	0.2	1/1	
1550940367	21.89 ± 0.19	21.620	1.00	15.7	50000	0.425	4/4	
91193988	3.6933 ± 0.0005	18.393	1.00	19.9	13597	0.249	2/2	
192991819	1.81005 ± 0.00018	34.905	1.00	35.9	7000	0.23	3/3	double-eclipse
73764818	0.135393 ± 3.2e-05	4.101	1.00	5.0	35994	0.464	1/1	
178539314	4.3923 ± 0.0011	5.228	1.00	7.8	8201	0.422	2/2	
938779482	0.4613 ± 0.0004	8.293	0.96	14.2	10000	0.2	1/1	double-eclipse
251903434	34.6 ± 1.9	109.202	0.98	28.1	7752	0.702	1/1	
159394587	14.753 ± 0.021	7.390	0.85	5.2	16890	0.6	1/4	
74342209	1.557 ± 0.004	146.008	0.87	44.0	9463	0.478	1/1	
1201364356	276.0 ± 6.0	483.909	0.86	20.9	12816	0.61	11/15	binary-disk?
398365709	8.0828 ± 0.0018	72.725	0.92	19.0	22570	0.54	5/5	DA+M
245830829	13.56 ± 0.15	300.596	0.96	18.7	17620	0.63	2/2	DA3+M
329670050	2.703 ± 0.011	99.642	0.98	34.9	9000	0.23	1/1	
243349100	23.447 ± 0.028	14.703	0.98	8.6	7250	0.23	5/6	
1920685932	25.12 ± 0.06	40.975	0.99	12.5	11981	0.388	1/2	binary
269663822	4.5085 ± 0.0008	226.862	0.98	75.2	7000	0.2	20/20	
403292348	3.3522 ± 0.0012	280.702	0.98	101.4	8000	0.2	2/2	
15131739	6.143 ± 0.004	17.562	0.99	16.5	31194	0.403	2/2	DA+L3
142616553	181.0 ± 1.7	31.440	0.84	19.0	14635	0.48	4/6	binary
901406326	0.113414 ± 2.2e-05	5.396	0.87	9.5	114711	0.701	1/1	
115013365	1.20234 ± 0.00005	6.454	1.00	9.0	12826	0.23	1/2	
269071459	21.51 ± 0.025	17.219	0.98	10.5	9375	0.852	5/5	
137607346	23.927 ± 0.025	190.904	0.98	58.7	9000	0.2	6/6	
458692929	27.4 ± 1.2	5.070	0.84	8.2	35105	0.36	1/1	DA+binary
311948770	16.932 ± 0.01	219.451	0.80	89.7	49650	0.66	5/5	DAO+M
903362877	65.4 ± 1.3	14.507	0.98	5.2	18344	0.488	1/3	binary
158747696	2.041 ± 0.007	23.570	0.98	27.8	8000	0.205	1/1	binary
8158475	56.85 ± 0.18	8.819	0.99	6.9	45333	0.527	1/2	
1990690286	15.322 ± 0.009	17.081	1.00	16.1	100000	0.48	2/2	
814547613	3.3579 ± 0.0006	27.264	0.96	19.8	14115	0.567	2/4	
88509155	128.0 ± 27.0	28.056	1.00	29.4	56610	0.53	1/1	DA+M
1951569775	92.9 ± 0.9	237.305	1.00	36.3	7000	0.2	2/2	
115075496	53.0 ± 4.0	9.833	1.00	9.9	44715	0.469	1/1	DA+M:

TIC	Period [h]	Amplitude [σ]	Like	$\langle$ Height [σ] $\rangle$	T_{eff} [K]	Mass [$M_\odot$]		info
118690168	34.85 ± 0.07	7.436	1.00	6.2	11023	0.587	2/3	
138653638	213.5 ± 2.6	40.343	0.78	17.0	12436	0.478	3/4	binary
721486224	150.0 ± 50.0	150.795	0.84	17.1	11692	0.725	3/3	binary
1101853877	121.0 ± 11.0	102.164	1.00	7.0	18791	0.673	1/2	DA+binary
453444667	82.1 ± 1.5	111.345	1.00	59.4	105000	0.75	2/2	DA+BP
246847488	173.0 ± 5.0	51.455	1.00	21.5	5720	0.1	1/1	
262548040	2* (0.10614391 ± 2.5e-7)	6.409	1.00	6.2	6230	0.41	3/5	DA7H
229098638	181.6 ± 0.7	815.491	1.00	19.2	18800	0.56	4/4	binary
404156391	28.133 ± 0.030	221.896	0.97	8.8	17770	0.542	2/2	binary
204440456	6.20 ± 0.07	18.679	1.00	21.3	6908	0.6018	1/1	
732235000	23.667 ± 0.020	19.728	1.00	8.5	19212	0.523	11/16	binary
50385872	5.4166 ± 0.0007	5.535	1.00	5.6	13141	0.710	2/8	
61965938	6.8168 ± 0.0013	51.961	1.00	5.1	19505	0.633	1/3	
1174761001	5.7114 ± 0.0018	23.495	1.00	24.2	18311	0.511	2/2	binary
23936802	5.8054 ± 0.0018	17.076	1.00	27.0	17146	0.269	4/4	
253936074	45.16 ± 0.07	25.890	1.00	5.5	29347	0.676	1/2	binary
2055541164	2.53003 ± 0.00023	73.753	1.00	48.6	23575	0.261	4/4	
408253347	7.9829 ± 0.0034	49.765	1.00	36.4	24466	0.47	2/3	DA+dMe
611305959	21.84 ± 0.05	21.142	1.00	16.4	90000	0.6	3/3	
611853501	0.385874 ± 0.000006	13.347	1.00	14.9	21697	1.055	2/2	
2024143938	1.1367 ± 0.0023	17.506	1.00	29.1	20000	0.323	1/1	DAZ+L3
380174982	4.4379 ± 0.0005	15.711	0.98	15.3	8607	0.83	3/3	
219099282	77.17 ± 0.20	22.276	1.00	6.3	45230	0.63	15/25	
610721330	0.671865 ± 0.000017	5.779	1.00	5.0	24332	1.218	1/4	
161820334	6.9232 ± 0.002	32.422	1.00	15.3	18462	0.183	6/7	
441702898	8.3222 ± 0.0029	13.601	0.99	8.6	7501	0.445	6/6	
144197100	0.245758 ± 0.000008	16.037	1.00	16.5	8595	0.87	2/2	
841424790	3.311 ± 0.0004	7.040	1.00	6.0	73027	0.751	3/7	

REFERENCES

2014, Society of Photo-Optical Instrumentation Engineers (SPIE) Conference Series, Vol. 9143, Space Telescopes and Instrumentation 2014: Optical, Infrared, and Millimeter Wave

Adams, W. S. 1915, PASP, 27, 236, doi: 10.1086/122440

Aerts, C., & Tkachenko, A. 2023, arXiv e-prints, arXiv:2311.08453, doi: 10.48550/arXiv.2311.08453

Amorim, L. L., Kepler, S. O., Külebi, B., Jordan, S., & Romero, A. D. 2023, ApJ, 944, 56, doi: 10.3847/1538-4357/acaf6e

Babcock, H. W. 1960, ApJ, 132, 521, doi: 10.1086/146960

Barstow, M. A., Jordan, S., O'Donoghue, D., et al. 1995, MNRAS, 277, 971, doi: 10.1093/mnras/277.3.971

Bell, K. J. 2020, in American Astronomical Society Meeting Abstracts, Vol. 235, American Astronomical Society Meeting Abstracts #235, 106.06

Bell, K. J., Hermes, J. J., Vanderbosch, Z., et al. 2017, The Astrophysical Journal, 851, 24, doi: 10.3847/1538-4357/aa9702

Bloecker, T. 1995, A&A, 297, 727

Böhm-Vitense, E. 1958, Zeitschrift fur Astrophysik, 46, 108

Bond, H. E., Kawaler, S. D., Ciardullo, R., et al. 1996a, AJ, 112, 2699, doi: 10.1086/118214

—. 1996b, AJ, 112, 2699, doi: 10.1086/118214

Bradley, P. A. 2001, The Astrophysical Journal, 552, 326, doi: 10.1086/320454

Brinkworth, C. S., Burleigh, M. R., Lawrie, K., Marsh, T. R., & Knigge, C. 2013, The Astrophysical Journal, 773, 47, doi: 10.1088/0004-637X/773/1/47

Caiazzo, I., Burdge, K. B., Fuller, J., et al. 2021, Nature, 595, 39, doi: 10.1038/s41586-021-03615-y

Calcaferro, Leila M., Córsico, Alejandro H., & Althaus, Leandro G. 2016, A&A, 589, A40, doi: 10.1051/0004-6361/201527996

Caldwell, D. A., Tenenbaum, P., Twicken, J. D., et al. 2020, Research Notes of the American Astronomical Society, 4, 201, doi: 10.3847/2515-5172/abc9b3

Castanheira, B. G., Kepler, S. O., Kleinman, S. J., Nitta, A., & Fraga, L. 2013, MNRAS, 430, 50, doi: 10.1093/mnras/sts474

Catalán, S., Isern, J., García-Berro, E., & Ribas, I. 2008, MNRAS, 387, 1693, doi: 10.1111/j.1365-2966.2008.13356.x

Choi, J., Dotter, A., Conroy, C., et al. 2016, ApJ, 823, 102, doi: 10.3847/0004-637X/823/2/102

Córsico, A. H., Uzundag, M., Kepler, S. O., et al. 2021a, A&A, 645, A117, doi: 10.1051/0004-6361/202039202

—. 2021b, A&A, 645, A117, doi: 10.1051/0004-6361/202039202

den Hartogh, J. W., Eggenberger, P., & Hirschi, R. 2019, A&A, 622, A187, doi: 10.1051/0004-6361/201834330

Diaz-Pinto, A., Garcia-Berro, E., Hernanz, M., Isern, J., & Mochkovitch, R. 1994, A&A, 282, 86

Doherty, C. L., Gil-Pons, P., Siess, L., Lattanzio, J. C., & Lau, H. H. B. 2014, Monthly Notices of the Royal Astronomical Society, 446, 2599, doi: 10.1093/mnras/stu2180

Dolez, N., Vauclair, G., Kleinman, S. J., et al. 2006, A&A, 446, 237, doi: 10.1051/0004-6361:20053149

Dominguez, I., Chieffi, A., Limongi, M., & Straniero, O. 1999, ApJ, 524, 226, doi: 10.1086/307787

Farihi, J., Robert, A., & Walters, N. 2023, A Nearby Polluted White Dwarf with a 6.2 h Spin Period. https://arxiv.org/abs/2312.03845

Fritzewski, D. J., Barnes, S. A., James, D. J., & Strassmeier, K. G. 2021, A&A, 652, A60, doi: 10.1051/0004-6361/202140894

Fu, J.-N., Dolez, N., Vauclair, G., et al. 2012, Monthly Notices of the Royal Astronomical Society, 429, 1585, doi: 10.1093/mnras/sts438

Fu, J.-N., Vauclair, G., Su, J., et al. 2019, Monthly Notices of the Royal Astronomical Society, 486, 3560, doi: 10.1093/mnras/stz1088

Fu, J.-N., Vauclair, G., Solheim, J.-E., et al. 2007, A&A, 467, 237, doi: 10.1051/0004-6361:20066295

Gaia Collaboration, Babusiaux, C., van Leeuwen, F., et al. 2018, A&A, 616, A10, doi: 10.1051/0004-6361/201832843

García-Berro, E., Isern, J., & Hernanz, M. 1997, Monthly Notices of the Royal Astronomical Society, 289, 973, doi: 10.1093/mnras/289.4.973

Gentile Fusillo, N. P., Tremblay, P. E., Cukanovaite, E., et al. 2021, MNRAS, 508, 3877, doi: 10.1093/mnras/stab2672

Giammichele, N., Fontaine, G., Brassard, P., & Charpinet, S. 2016, The Astrophysical Journal Supplement Series, 223, 10, doi: 10.3847/0067-0049/223/1/10

Greiss, S., Gänsicke, B. T., Hermes, J. J., et al. 2014, Monthly Notices of the Royal Astronomical Society, 438, 3086, doi: 10.1093/mnras/stt2420

Guo, J., Zhao, J., Zhang, H., et al. 2022, MNRAS, 509, 2674, doi: 10.1093/mnras/stab3151

Heger, A., Langer, N., & Woosley, S. E. 2000, ApJ, 528, 368, doi: 10.1086/308158

Heger, A., Woosley, S. E., & Spruit, H. C. 2005, ApJ, 626, 350, doi: 10.1086/429868

Henyey, L., Vardya, M. S., & Bodenheimer, P. 1965, ApJ, 142, 841, doi: 10.1086/148357

Hermes, J. J., Kawaler, S. D., Bischoff-Kim, A., et al. 2017a, The Astrophysical Journal, 835, 277, doi: 10.3847/1538-4357/835/2/277

Hermes, J. J., Gänsicke, B. T., Kawaler, S. D., et al. 2017b, ApJS, 232, 23, doi: 10.3847/1538-4365/aa8bb5

Higgins, M. E., & Bell, K. J. 2023, AJ, 165, 141, doi: 10.3847/1538-3881/acb20c

Höfner, S., & Olofsson, H. 2018, A&A Rv, 26, 1, doi: 10.1007/s00159-017-0106-5

Jermyn, A. S., Bauer, E. B., Schwab, J., et al. 2023, ApJS, 265, 15, doi: 10.3847/1538-4365/acae8d

Kawaler, S. D. 2015, in Astronomical Society of the Pacific Conference Series, Vol. 493, 19th European Workshop on White Dwarfs, ed. P. Dufour, P. Bergeron, & G. Fontaine, 65, doi: 10.48550/arXiv.1410.6934

Kawaler, S. D., O'Brien, M. S., Clemens, J. C., et al. 1995, ApJ, 450, 350, doi: 10.1086/176145

Kepler, S., & Romero, A. D. 2017, EPJ Web Conf., 152, 01011, doi: 10.1051/epjconf/201715201011

Kepler, S. O. 1993, Baltic Astronomy, 2, 515, doi: 10.1515/astro-1993-3-425

Kepler, S. O., Kleinman, S. J., Nitta, A., et al. 2007, MNRAS, 375, 1315, doi: 10.1111/j.1365-2966.2006.11388.x

Kepler, S. O., Koester, D., Pelisoli, I., Romero, A. D., & Ourique, G. 2021, Monthly Notices of the Royal Astronomical Society, 507, 4646, doi: 10.1093/mnras/stab2411

Kepler, S. O., Koester, D., Pelisoli, I., Romero, A. D., & Ourique, G. 2021, MNRAS, 507, 4646, doi: 10.1093/mnras/stab2411

Kepler, S. O., Robinson, E. L., & Nather, R. E. 1983, ApJ, 271, 744, doi: 10.1086/161241

Kepler, S. O., Giovannini, O., Wood, M. A., et al. 1995a, ApJ, 447, 874, doi: 10.1086/175924

—. 1995b, ApJ, 447, 874, doi: 10.1086/175924

Kilic, M., Bergeron, P., Kosakowski, A., et al. 2020, ApJ, 898, 84, doi: 10.3847/1538-4357/ab9b8d

Kilic, M., Stanek, K. Z., & Pinsonneault, M. H. 2007, ApJ, 671, 761, doi: 10.1086/522228

Kochukhov, O. 2011, in Physics of Sun and Star Spots, ed. D. Prasad Choudhary & K. G. Strassmeier, Vol. 273, 249–255, doi: 10.1017/S1743921311015328

Krtička, J., Kawka, A., Mikulášek, Z., et al. 2023, Astronomy &amp Astrophysics, 674, A94, doi: 10.1051/0004-6361/202245551

Kurtz, D. W., Shibahashi, H., Murphy, S. J., Bedding, T. R., & Bowman, D. M. 2015, MNRAS, 450, 3015, doi: 10.1093/mnras/stv868

Labadie-Bartz, J., Hümmerich, S., Bernhard, K., Paunzen, E., & Shultz, M. E. 2023, A&A, 676, A55, doi: 10.1051/0004-6361/202346657

Langer, N. 2012, Annual Review of Astronomy and Astrophysics, 50, 107, doi: 10.1146/annurev-astro-081811-125534

Li, C., Fu, J., Fox-Machado, L., Su, J., & Chen, F. 2017, NewA, 55, 48, doi: 10.1016/j.newast.2017.03.003

Lightkurve Collaboration, Cardoso, J. V. d. M., Hedges, C., et al. 2018, Lightkurve: Kepler and TESS time series analysis in Python. http://ascl.net/1812.013

Marsh, T. R., Dhillon, V. S., & Duck, S. R. 1995, MNRAS, 275, 828, doi: 10.1093/mnras/275.3.828

McCook, G. P., & Sion, E. M. 2016, VizieR Online Data Catalog, 1, 2035

Molnár, L., Szabó, R., & Plachy, E. 2016, JAAVSO, 44, 168, doi: 10.48550/arXiv.1610.02004

Moss, A., Kilic, M., Bergeron, P., Firgard, M., & Brown, W. 2023, MNRAS, 523, 5598, doi: 10.1093/mnras/stad1835

Mosser, B., Goupil, M. J., Belkacem, K., et al. 2012, A&A, 548, A10, doi: 10.1051/0004-6361/201220106

Moyano, F. D., Eggenberger, P., Meynet, G., et al. 2022, A&A, 663, A180, doi: 10.1051/0004-6361/202243389

Moyano, F. D., Eggenberger, P., Salmon, S. J. A. J., Mombarg, J. S. G., & Ekström, S. 2023, A&A, 677, A6, doi: 10.1051/0004-6361/202346548

Nather, R. E., Winget, D. E., Clemens, J. C., Hansen, C. J., & Hine, B. P. 1990, ApJ, 361, 309, doi: 10.1086/169196

O'Brien, M. W., Tremblay, P. E., Gentile Fusillo, N. P., et al. 2023, MNRAS, 518, 3055, doi: 10.1093/mnras/stac3303

Oliveira da Rosa, G., Kepler, S. O., Córsico, A. H., et al. 2022, ApJ, 936, 187, doi: 10.3847/1538-4357/ac8871

Østensen, R. H., Bloemen, S., Vučković, M., et al. 2011, ApJL, 736, L39, doi: 10.1088/2041-8205/736/2/L39

Paxton, B., Bildsten, L., Dotter, A., et al. 2011, ApJS, 192, 3, doi: 10.1088/0067-0049/192/1/3

Paxton, B., Cantiello, M., Arras, P., et al. 2013, ApJS, 208, 4, doi: 10.1088/0067-0049/208/1/4

Paxton, B., Marchant, P., Schwab, J., et al. 2015, ApJS, 220, 15, doi: 10.1088/0067-0049/220/1/15

Paxton, B., Schwab, J., Bauer, E. B., et al. 2018, ApJS, 234, 34, doi: 10.3847/1538-4365/aaa5a8

Paxton, B., Smolec, R., Schwab, J., et al. 2019, ApJS, 243, 10, doi: 10.3847/1538-4365/ab2241

Pech, D., & Vauclair, G. 2006, A&A, 453, 219, doi: 10.1051/0004-6361:20054370

Pedersen, M. G., & Bell, K. J. 2023, AJ, 165, 239, doi: 10.3847/1538-3881/accc31

Pfeiffer, B., Vauclair, G., Dolez, N., et al. 1996, A&A, 314, 182

Poelarends, A. J. T., Herwig, F., Langer, N., & Heger, A. 2008, The Astrophysical Journal, 675, 614, doi: 10.1086/520872

Reimers, D. 1975, Memoires of the Societe Royale des Sciences de Liege, 8, 369

Rohrmann, R. D., Althaus, L. G., & Kepler, S. O. 2011, MNRAS, 411, 781, doi: 10.1111/j.1365-2966.2010.17716.x

Romero, A. D., Campos, F., & Kepler, S. O. 2015, MNRAS, 450, 3708, doi: 10.1093/mnras/stv848

Romero, A. D., Kepler, S. O., Hermes, J. J., et al. 2022, Monthly Notices of the Royal Astronomical Society, 511, 1574, doi: 10.1093/mnras/stac093

Siess, L. 2010, A&A, 512, A10, doi: 10.1051/0004-6361/200913556

Su, J., Li, Y., Fu, J.-N., & Li, C. 2013, Monthly Notices of the Royal Astronomical Society, 437, 2566, doi: 10.1093/mnras/stt2069

Tremblay, P. E., Hollands, M. A., Gentile Fusillo, N. P., et al. 2020, MNRAS, 497, 130, doi: 10.1093/mnras/staa1892

Wenger, M., Ochsenbein, F., Egret, D., et al. 2000, A&AS, 143, 9, doi: 10.1051/aas:2000332

Williams, K. A., Hermes, J. J., & Vanderbosch, Z. P. 2022, AJ, 164, 131, doi: 10.3847/1538-3881/ac8543

Woosley, S. E., & Heger, A. 2015, The Astrophysical Journal, 810, 34, doi: 10.1088/0004-637X/810/1/34

Zahn, J. P. 1977, A&A, 57, 383